Heliyon 10 (2024) e35483

Contents lists available at ScienceDirect

Heliyon

journal homepage: www.cell.com/heliyon

Research article

Elucidating the effects of nitrogen and phosphorus co-doped carbon on complex spinel $NiFe_2O_4$ towards oxygen reduction reaction in alkaline media

Siyabonga Patrick Mbokazi [a], Thabo Matthews [a], Haitao Zheng [b], Makhaokane Paulina Chabalala [a], Memory Zikhali [a], Kudzai Mugadza [a], Sandile Gwebu [a], Lukhanyo Mekuto [c], Nobanathi Wendy Maxakato [a,*]

[a] Department of Chemical Sciences, University of Johannesburg, Doornfontein, 2028, South Africa
[b] Energy Centre, Council for Scientific and Industrial Research (CSIR), Pretoria, 0001, South Africa
[c] Department of Chemical Engineering, School of Mining, Metallurgy, and Chemical Engineering, Faculty of Engineering and the Built Environment, University of Johannesburg, Doornfontein, 2006, South Africa

A B S T R A C T

The study presents for the first time complex spinel $NiFe_2O_4$ nanoparticles supported on nitrogen and phosphorus co-doped carbon nanosheets (NPCNS) prepared using sol gel and the carbonization of graphitic carbon nitride with lecithin as a highly active and durable electrocatalyst for oxygen reduction reaction. The physicochemical properties of complex spinel $NiFe_2O_4$ on NPCNS and subsequent nanomaterials were investigated using techniques such as X-ray diffraction, Fourier transform infrared spectroscopy, X-ray photoelectron spectroscopy, and transmission electron microscopy. The electrochemical activity of the electrocatalysts was evaluated using hydrodynamic linear sweep voltammetry, cyclic voltammetry, electrochemical impedance spectroscopy, and chronoamperometry. The electrocatalytic performance of the $NiFe_2O_4$/NPCNS nanohybrid electrocatalyst is dominated by the $4e^-$ transfer mechanism, with an onset potential of 0.92 V vs. RHE, which is closer to that of the Pt/C, and a current density of 7.81 mA/cm^2 that far exceeds that of the Pt/C. The nanohybrid demonstrated the best stability after 14 400 s, outstanding durability after 521 cycles, and the best ability to oxidize methanol and remove CO from its active sites during CO tolerance studies. This improved catalytic activity can be attributed to small nanoparticle sizes of the unique complex spinel nickel ferrite structure, N-Fe/Ni coordination of nanocomposite, high dispersion, substantial ECSA of 47.03 mF/cm^2, and synergy caused by strong metal-support and electronic coupling interactions.

1. Introduction

Fuel cells are a potential alternative to fossil fuels due to their efficiency, affordability, and eco-friendliness [1,2]. However, the slow kinetics of the oxygen reduction reaction (ORR) pose challenges for commercialization [3–5]. Researchers are working on developing non-noble metal catalysts consisting of Ni, Co, and Fe, which have high stability, follow a four-electron pathway, have high CO tolerance, and are cost-effective [6–8]. Non-precious metal oxides, e.g., Fe_2O_3, Fe_3O_4, NiO, and Co_3O_4, and multi-complex oxides have also gained attention due to their high abundance, low cost, and good ORR activity [9,10,59,60].

Kiani's research on inverse spinel magnesium ferrites infused with heteroatom co-doped carbon nanocomposites revealed that high annealing temperatures significantly enhanced the catalytic activity towards ORR. This synergistic effect, as reported by Kiani et al. [15], is crucial for the successful synthesis of spinel ferrites with heteroatom co-doped carbon nanocomposites. The combination of these components and synthetic parameters leads to increased crystallinity and enhanced specific surface area, ultimately improving

* Corresponding author.
E-mail address: nmaxakato@uj.ac.za (N.W. Maxakato).

https://doi.org/10.1016/j.heliyon.2024.e35483
Received 18 February 2024; Received in revised form 18 July 2024; Accepted 30 July 2024
Available online 30 July 2024
2405-8440/

the ORR performance [16]. Zhang et al. [17] studied the effect of pyrolysis temperature on nitrogen-doped carbon nanoflowers for ORR. It was deduced that high annealing temperatures led to a larger surface area, active N sites, and pore structure, resulting in superior ORR activity and enhanced durability.

Spinel ferrites of the formula MFe_2O_4, where M represents Mg^{2+}, Co^{2+}, Ni^{2+}, Zn^{2+}, and Mn^{2+} divalent ions are being researched due to their excellent methanol tolerance, acceptable catalytic activity, and durability in alkaline media [11,12,23]. Compared with large sized nanomaterials, spinel ferrites have superior mechanical, thermal, and electrical properties. However, the catalytic activity of pure, unsupported spinel ferrites is limited by poor electron mobility and low electrical conductivity. In the past few years, researchers have focused on exploring synthetic strategies that could result in spinel ferrites with controlled morphologies, limited agglomeration, regulated nanoparticle sizes, and lattice integrity [62].

Inverse spinel ferrites have been extensively studied for oxygen reduction reaction. Go et al. [63] reported on the synthesis of an oxygen vacancy rich $CoFe/CoFe_2O_4$ nanostructure embedded in N-doped hollow carbon spheres (V_o-$CoFe/CoFe_2O_4$@NC) through pyrolysis, carbonization, and partial reduction. The outstanding ORR activity was attributed to the well-defined heterointerfaces and moderately controlled electronic structure between the CoFe alloy and inverse spinel $CoFe_2O_4$ nanoparticles. Qin et al. [14] elucidated the interfacial N-Ni coordination on inverse spinel $NiFe_2O_4$/N-doped graphene hybrids as the activity descriptor for ORR on that nanomaterial.

$NiFe_2O_4$ cubic nanostructures are commonly used in magnetic technologies, sensors, and adsorption science, but their potential in ORR remains untapped [13]. Recent research shows that inverse spinel $NiFe_2O_4$ combined with carbon nanomaterials exhibits better conductivity and superior ORR activity than Pt/C [14]. However, complex spinel nickel ferrite implanted on these nanocomposites have not been mentioned in the literature in the past few years.

This study explores the potential use of multi-atom catalysts in energy conversion, focusing on the synthesis of complex spinel $NiFe_2O_4$ on nitrogen and phosphorus co-doped carbon (NPCNS) nanohybrid for ORR. The synthesis involves sol-gel coupling with the carbonization of graphitic carbon nitride (gC_3N_4) and lecithin. gC_3N_4 serves as a carbon/nitrogen source and self-sacrificing template, while lecithin from egg yolk acts as a carbon/phosphorus source. The amphiphilic structure of lecithin forms a phospholipid membrane around the gC_3N_4 lamellar structure, incorporating $NiFe_2O_4$ metal precursors and citric acid. Complex spinel $NiFe_2O_4$ nanoparticles are formed on NPCNS after annealing and carbonization. $NiFe_2O_4$/NPCNS demonstrates high ORR efficiency, numerous electrochemical active sites, long-term stability, and resistance to CO poisoning, suggesting its potential suitability for future direct methanol fuel cell (DMFC) applications.

2. Experimental section

2.1. Materials

The chemicals, including $Ni(NO_3)_2{\cdot}6H_2O$, $Fe(NO_3)_3{\cdot}9H_2O$, KOH, and citric acid ($C_6H_80_7$) anhydrous extra pure 99 %, were obtained from Sisco Research Laboratories and used without additional purification. Polyvinylpyrrolidone (PVP) was purchased from Sigma Aldrich and utilized without further processing. Nafion 10 %, and absolute ethanol 99.9 % were acquired from Merck Aldrich and employed as received, without additional purification. Pt/C (20 wt%) XC-72 was purchased from The Fuel Cell Store and used without further purification.

2.2. Synthesis procedure

2.2.1. Extraction of lecithin from egg yolk and synthesis of bulk gC_3N_4

Eggs purchased from Shoprite in South Africa were used to extract lecithin. The process involved separating an egg yolk, mixing it with 250 mL of ethanol, stirring for an hour, and then allowing the mixture to settle in a separating funnel for 2 hours. The supernatant was collected, and ethanol was evaporated to obtain a golden lecithin paste [4]. Additionally, bulk gC_3N_4 was produced by heating melamine in a tube furnace, ramping up the temperature to 600 °C at a rate of 2 °C min^{-1}, holding it for 2 h under an Ar atmosphere, and then naturally cooling to room temperature.

2.2.2. Synthesis of NPCNS, $NiFe_2O_4$/NPCNS, Fe_2O_3/NPCNS, NiO/NPCNS, $NiFe_2O_4$/PCNS, and $NiFe_2O_4$/NCNS

N- and P-co-doped graphitic carbon nanosheets (NPCNS) were synthesized by combining 0.8 g of lecithin and 1.2 g of gC_3N_4 in 20 mL of distilled water. After stirring for 1 hour, water was evaporated, resulting in a solid mixture that was crushed to form a well-mixed plasticine-like pale yellow block. The solid was then calcined in a tube furnace, ramping from ambient temperature to 1000 °C at a rate of 3.3 °C min^{-1} in an Ar environment, and held for 2 hours. NPCNS were obtained after cooling to ambient temperature.

In a standard synthesis process, a mixture of 0.8 g lecithin and 1.2 g gC_3N_4 in 20 mL of distilled water was stirred for 1 hour. A dark yellow solution containing 0.8 g $Fe(NO_3)_3{\cdot}9H_2O$, 0.4 g $Ni(NO_3)_2{\cdot}6H_2O$, 1.2 g citric acid, 0.2 g PVP, and 20 mL of distilled water was then added dropwise to the lecithin-gC_3N_4 solution and stirred for an additional hour. Citric acid acted as a chelating agent for $NiFe_2O_4$ synthesis, and PVP controlled particle size. After gradual water evaporation under a water bath, the resulting solid mixture was crushed to form a well-mixed plasticine-like yellow block. The solid was calcined in a tube furnace from room temperature to 1000 °C at 3.3 °C min^{-1} under an Ar atmosphere for 2 hours. $NiFe_2O_4$ nanoparticles impregnated onto N- and P-co-doped graphitic carbon nanosheets (NPCNS) were obtained upon cooling. Similar procedures were applied for the synthesis of Fe_2O_3/NPCNS and NiO/NPCNS, using $Fe(NO_3)_3{\bullet}9H_2O$ and $Ni(NO_3)_2{\bullet}6H_2O$ as metal precursors. Additionally, $NiFe_2O_4$/PCNS and $NiFe_2O_4$/NCNS were synthesized using lecithin and graphitic carbon nitride as the sole carbon source precursors, following the same route.

2.3. Material characterization

SEM images were recorded on FEI Nova 68 Nano SEM 450; TEM images were collected on a TEM-JEM-2010 instrument; XRD patterns were recorded on a Bruker D2 Phaser with Co-Kα radiation (λ = 0.15443 nm). X-ray photoelectron spectroscopy (XPS) of $NiFe_2O_4$/NPCNS and NiO/NPCNS was acquired on a Thermo Scientific (ESCAlab 250Xi) equipped with a monochromatic Al α (1486.7 eV) with beam size and power of 900 μ m and 300 W, and XPS measurements for Fe_2O_3/NPCNS were collected by a PHOIBOS 150 hemispherical electron energy analyser with a monochromatic Al x-ray source used with a photon energy of 1486.71 eV; FTIR measurements for all the electrocatalysts were performed on the PerkinElmer FTIR spectrophotometer. RAMAN spectra were collected using a Thermo Scientific DXR2 Smart Raman equipped with a 532 nm laser source. Nitrogen adsorption isotherms were performed using an ASAP Tristar II 3020 physisorption analyzer.

2.4. Electrochemical measurements

Electrochemical oxygen reduction reaction (ORR) measurements were conducted at room temperature using a Metrohm Autolab 320N and Metrohm Dropsens µStat-i 400 potentiostat. Electrochemical impedance spectroscopy (EIS) studies utilized the Gamry interface 1010E, 27 143 potentiostat/galvanostat. A three-electrode system was employed, comprising a rotating disk electrode (RDE; 6.1204.300 GC, 0.060 cm^2 geometric surface area), a platinum wire counter electrode, and an Ag/AgCl reference electrode (3 M KCl saturated). The RDE underwent cleaning via alumina slurry polishing with varying particle sizes (0.05 µm–5 µm) on a polishing cloth, followed by rinsing with distilled water. The rotation speed of the working electrode was controlled for hydrodynamic studies using a fixed rotator.

The polished and dried working electrode (WE) was placed on a specialized electrode pedestal for electrocatalyst coating. The electrocatalyst ink was prepared with 10 mg of electrocatalyst powder, 900 µL of water, 50 µL of dimethylformamide (DMF), and 50 µL of 5 % Nafion. DMF, with its high boiling point and low surface tension, facilitated even spreading on the electrode surface, ensuring homogeneous material deposition. The mixture was ultrasonicated in an ice-cold bath for 20–30 min to ensure homogeneity and minimize bubble formation. Subsequently, 10 µL of the catalyst ink was drop-cast on the WE and dried at room temperature. The polarization curves for the electrocatalytic oxygen reduction reaction were acquired without employing iR compensation.

All the ORR measurements were carried out in an O_2/Ar saturated 0.1 M KOH solution at room temperature. All potentials were

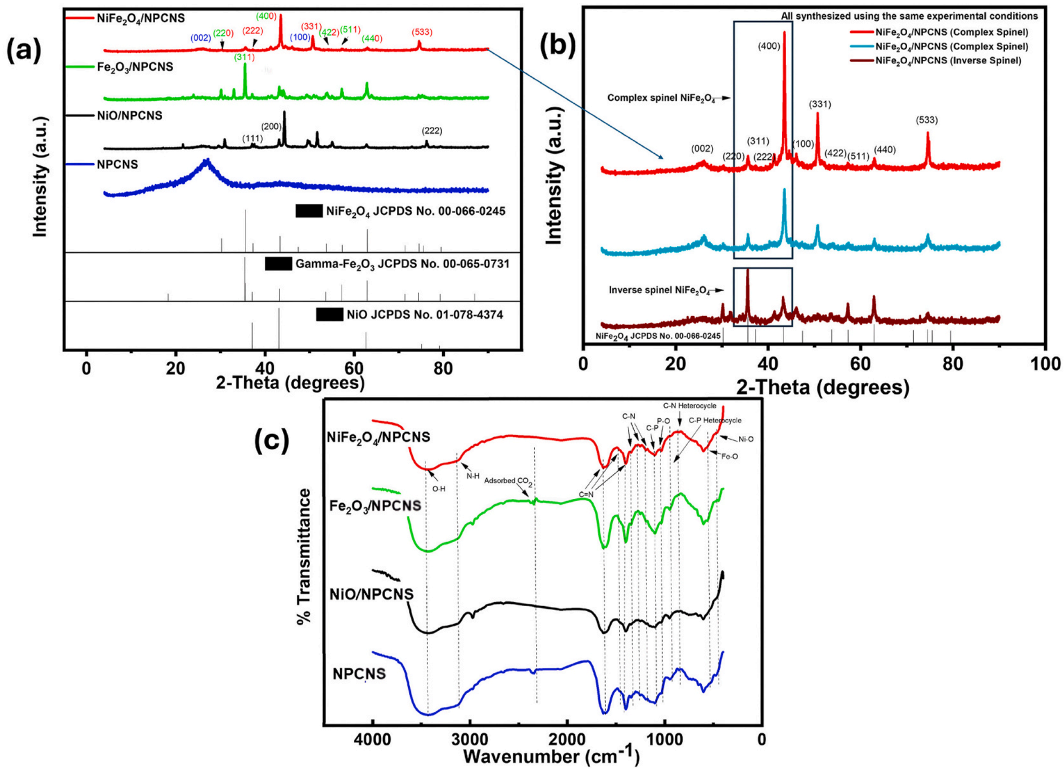

Fig. 1. (a) X-ray diffraction patterns of $NiFe_2O_4$/NPCNS, Fe_2O_3/NPCNS, NiO/NPCNS, and NPCNS hybrid nanomaterials, (b) X-ray diffraction patterns of $NiFe_2O_4$/NPCNS prepared using the same experimental conditions and subjected to X-ray diffraction analysis after synthesis to show that the preparation method results in complex spinel $NiFe_2O_4$ nanoparticles on NPCNS and, (c) FTIR spectra of $NiFe_2O_4$/NPCNS, Fe_2O_3/NPCNS, NiO/NPCNS, and NPCNS hybrid nanomaterials,.

converted to reverse hydrogen electrodes (RHE) using the equation:

$E_{(RHE)} = E_{(Ag/AgCl)} + 0.197 + (0.059*pH)$

The Koutecky-Levich equation was used to calculate the transferred electrons based on ORR LSV curves obtained at different rotation speeds.

$$\frac{1}{J}=\frac{1}{J_K}+\frac{1}{J_L}$$

$$J_K = nFkC_{O_2} \text{ and } I_L = 0.62\, nFC_{O_2}D_{O_2}^{\frac{2}{3}}v^{\frac{-1}{6}}\omega^2$$

$$B = 0.62\, nFC_{O_2}D_{O_2}^{\frac{2}{3}}v^{\frac{-1}{6}} \rightarrow n = \frac{B}{0.62FC_{O2}D_{O2}^{2/3}v^{-1/6}}$$

In the given equations, J represents the total observed current density (mA/cm^2), with J_K as the kinetic current density, J_L as the diffusion-limited current density, and I_L as the limiting current density (mA/cm^2). Other variables include n (number of electrons transferred), F (Faraday's constant, 96 485C/mol), C_{O2} (bulk O_2 concentration in 0.1 M KOH electrolyte solution, 1.26×10^{-6} mol/cm^3), D_{O2} (diffusion coefficient of O_2, 1.98×10^{-5} cm^2/s), and v (kinetic viscosity of the solution, 0.01 cm^2/s).

3. Results and discussion

3.1. Crystallographic and surface analysis studies

The XRD analysis in Fig. 1(a) investigated hybrid nanomaterials' phase composition and crystal structures. The interplanar spacing, d, for (002) was found to be between 3.49 and 3.65 Å (Table S1), slightly higher than undoped graphitic carbon nitride (3.44 Å). This suggests the presence of doped phosphorus atoms between graphitic carbon nanosheet layers [4,21,24]. The high crystallinity of all the composites was indicated by the average crystal sizes and lattice parameters, as shown in Table S1. All the nanomaterials had similar XRD spectra for the (002) and (100) planes, with the strongest diffraction peaks at 2θ degrees of 25.06°, 25.46°, 25.33°, and 24.37° for $NiFe_2O_4$/NPCNS, Fe_2O_3/NPCNS, NiO/NPCNS, and NPCNS, respectively as shown in Fig. 1 and Fig. S1. These peaks indicate that the spacing of the graphitized layers on all catalysts is much bigger than that of undoped gC_3N_4 [4]. gC_3N_4 was doped with phosphorus and metal oxides were introduced on the surface of the carbon support which increased the interlayer spacing. Furthermore, high thermal treatments implemented in this study resulted in the creation of defects on gC_3N_4 which disrupted the regular stacking of the resulting carbon support and resulted in increased interlayer spacing.

The synthesis of FCC complex spinel $NiFe_2O_4$ nanoparticles on NPCNS was confirmed by well-resolved diffraction peaks located at 2θ degrees of 30.4° (220), 35.9° (311), 37.2° (222), 43.3° (400), 50.6° (331), 54.1° (422), 57.5° (511), 63.0° (440), and 74.8° (533), indexed to JCPDS No. 00-066-0245 as depicted in Fig. 1 (a & b). The formation of complex spinel $NiFe_2O_4$ was further confirmed by synthesizing $NiFe_2O_4$/NPCNS three times using the same experimental conditions underlined in this study and then subjecting those samples to XRD analysis. As seen in Fig. 1 (b), The first two samples resulted in complex $NiFe_2O_4$ on NPCNS since the (400) and (331) miller planes had higher intensity than the (311) plane. High thermal temperatures (1000 °C) or even higher temperatures can result in cation redistribution from the octahedral site to the tetrahedral site and vice versa [64]. This phenomenon resulted in the transformation of the inverse spinel $NiFe_2O_4$ nanostructure to a complex spinel $NiFe_2O_4$ nanostructure on NPCNS. The last sample showed an inverse spinel $NiFe_2O_4$ on NPCNS which means that the synthetic method followed under this study can also result in the formation of inverse spinel $NiFe_2O_4$, so optimization of the synthetic parameters is needed to result in only complex $NiFe_2O_4$ on NPCNS. Gamma-Fe_2O_3 nanoparticles were successfully incorporated on NPCNS, as indicated by the appearance of corresponding diffraction peaks of hematite at 2θ degrees of 30.1° (220), 35.3° (311), 54.0° (422), 57.4° (551), and 63.3° (440), indexed to JCPDS No. 00-065-0731. The NiO nanoparticles on NPCNS were identified by diffraction peaks at 37.6° (111), 44.6° (200), and 76.3° (222), with peak intensity and relative peak position corresponding to JCPDS No. 01-078-4374.

The FTIR spectra in Fig. 1(c) confirmed the coordination between metals, chemical composition, and bonding information of hybrid nanomaterials. The stretching vibration signals of aromatic heptazine-derived repeating units were observed in the region of 1200 cm^{-1} to 1600 cm^{-1}, including sp^2 hybridized C=N stretching modes and out-of-plane stretching vibrations of the sp^3 C–N bonds. A characteristic breathing mode of the s-triazine C–N heterocycles was attributed to the adsorption peak centered at approximately 864 cm^{-1} [18].

The study found that the peaks observed at different wavelengths in the FTIR spectrum were attributed to various chemical bonds and modes. These included the N–H amino groups (at 934 cm^{-1}), residual N–H (at 3125 cm^{-1}), O–H group (at 3463 cm^{-1}), P–O bonds (at 1027 cm^{-1}), C–P bonds (at 1106 cm^{-1}), and metal oxide bonds (around 456 cm^{-1} and 561 cm^{-1}). The intensity of some peaks related to C–N (at 1200 cm^{-1}, 1252 cm^{-1}, and 1358 cm^{-1}) was reduced due to the displacement of carbon atoms by phosphorus atoms to form P–C bonds [19–21]. Furthermore, a peak at 939 cm^{-1} was attributed to the C–P heterocycle. Successful co-doping was pre-confirmed by FTIR and further confirmed by XPS. The FTIR also showed absorption peaks between 2297 cm^{-1} and 2441 cm^{-1} due to CO_2 sorption molecules at the surface [22]. The presence of hydroxyls, amines, or other polar groups on the surface of Fe_2O_3/NPCNS lead to the adsorption of CO_2 via chemisorption and physisorption mechanisms since samples were prepared in air before FTIR analysis.

The morphology of the synthesized hybrid nanocomposites was analyzed via SEM. Fig. 2 demonstrated well-defined carbon nanosheets in all hybrids. Incorporating metal oxides into carbon supports can improve the surface area, porosity, and adsorption capacity of carbon nanomaterials [47,48]. Metal oxides can introduce micro- and mesoporosity into the carbon structure by enhancing the thermal stability of carbon nanostructures, allowing for higher temperature treatments which can increase surface area. Complex spinel $NiFe_2O_4$, Gamma-Fe_2O_3, and NiO nanoparticles were successfully dispersed on the carbon support, as shown in Fig. 2(a, b, c). Additionally, enfolded and co-doped carbon nanosheets were synthesized successfully, as shown in Fig. 2(d).

The carbon nanosheets have nitrogen-substituted heteroatoms that create a π-conjugated system of graphitic planes due to sp^2 hybridization between carbon and nitrogen atoms, as shown by SEM studies. The addition of phosphorus to these nanosheets results in a change in the electrical structure, leading to a new structure (NPCNS) with unique features. This explains the similar morphological characteristics of all nanocomposites.

The SEM elemental mapping images in Fig. 2 show an even distribution of C, N, P, Fe, Ni, and O elements in $NiFe_2O_4$/NPCNS, indicating the presence of phosphorus and nitrogen heteroatoms and complex spinel ferrite nanoparticles on the co-doped carbon support. SEM elemental mapping for Fe_2O_3/NPCNS, NiO/NPCNS, and NPCNS are shown in Fig. S2, confirming the respective elements present in each nanohybrid.

Energy dispersive X-ray spectroscopy (EDS) shown in Fig. S3 revealed peaks for P, N, and C, which confirms the presence of the heteroatoms used for doping the carbon support (NPCNS) on all the nanocomposites. $NiFe_2O_4$/NPCNS showed peaks for Fe, Ni, and O, which confirmed the presence of those components, alluding to the successful incorporation of the complex spinel $NiFe_2O_4$ nanoparticles. EDS was also used to confirm respective elements of the metal oxides on NiO/NPCNS and Fe_2O_3/NPCNS as shown on Fig. S3.

The morphology and structure of composites were examined using TEM, revealing that $NiFe_2O_4$, Fe_2O_3, and NiO nanoparticles remained tightly and uniformly decorated on NPCNS post-calcination and carbonization as shown in Fig. 3(a–c, e). The adhesion forces between the nanoparticles and carbon support, including van der Waals forces, electrostatic forces, and chemical bonds, contribute to the composites' good chemical and environmental stability [58]. The nanomaterials were polycrystalline, as shown by the SAED pattern inserts in Fig. 3(a–c, e, g), and the corresponding miller indices are presented in Table S2.

The concentric diffraction rings observed in $NiFe_2O_4$/NPCNS correspond to the (311), (400), and (533) planes of the $NiFe_2O_4$ spinel structure. In Fe_2O_3/NPCNS and $NiFe_2O_4$/NPCNS, four rings are assigned to the (220), (311), (422), and (440) planes of the Fe_2O_3 hematite and complex spinel $NiFe_2O_4$ spinel. For NiO/NPCNS, three rings are associated with the (111), (200), and (222) planes of NiO hematite. Two rings on (002) and (100), characteristic of graphite-carbon, are identified for the carbon support. These results from selected area electron diffraction (SAED) are consistent with X-ray diffraction (XRD) patterns.

The metal oxides dispersed on NPCNS exhibited uniformity during the synthesis process, as evidenced by their similar particle size distributions in Fig. 3(b, d, and f). The $NiFe_2O_4$/NPCNS had a smaller particle size distribution compared to Fe_2O_3/NPCNS indicating that the carbon nanosheets prevented agglomeration due to the dispersion effect, making the former composite more effective for ORR

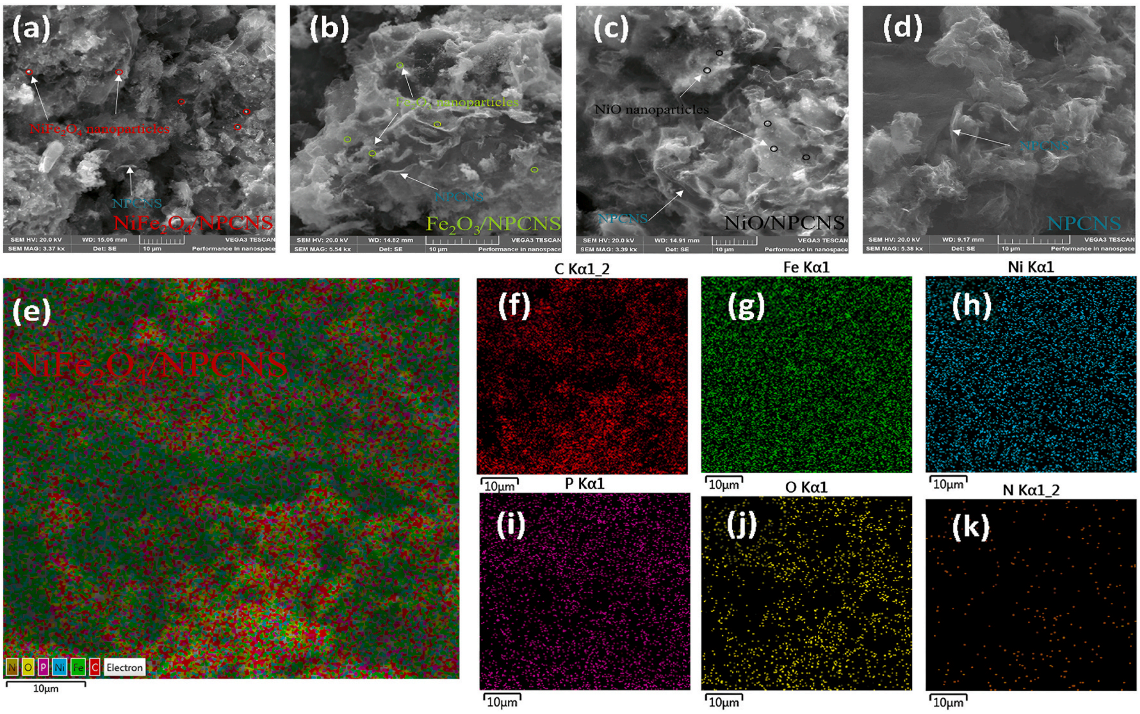

Fig. 2. SEM micrographs for (a) $NiFe_2O_4$/NPCNS, (b) Fe_2O_3/NPCNS, (c) NiO/NPCNS, (d) NPCNS, and elemental mapping of (e) $NiFe_2O_4$/NPCNS showing the (f) C, (g) Fe, (h) Ni, (i) P, (j) O, and (k) N respective elements on that hybrid nanomaterial.

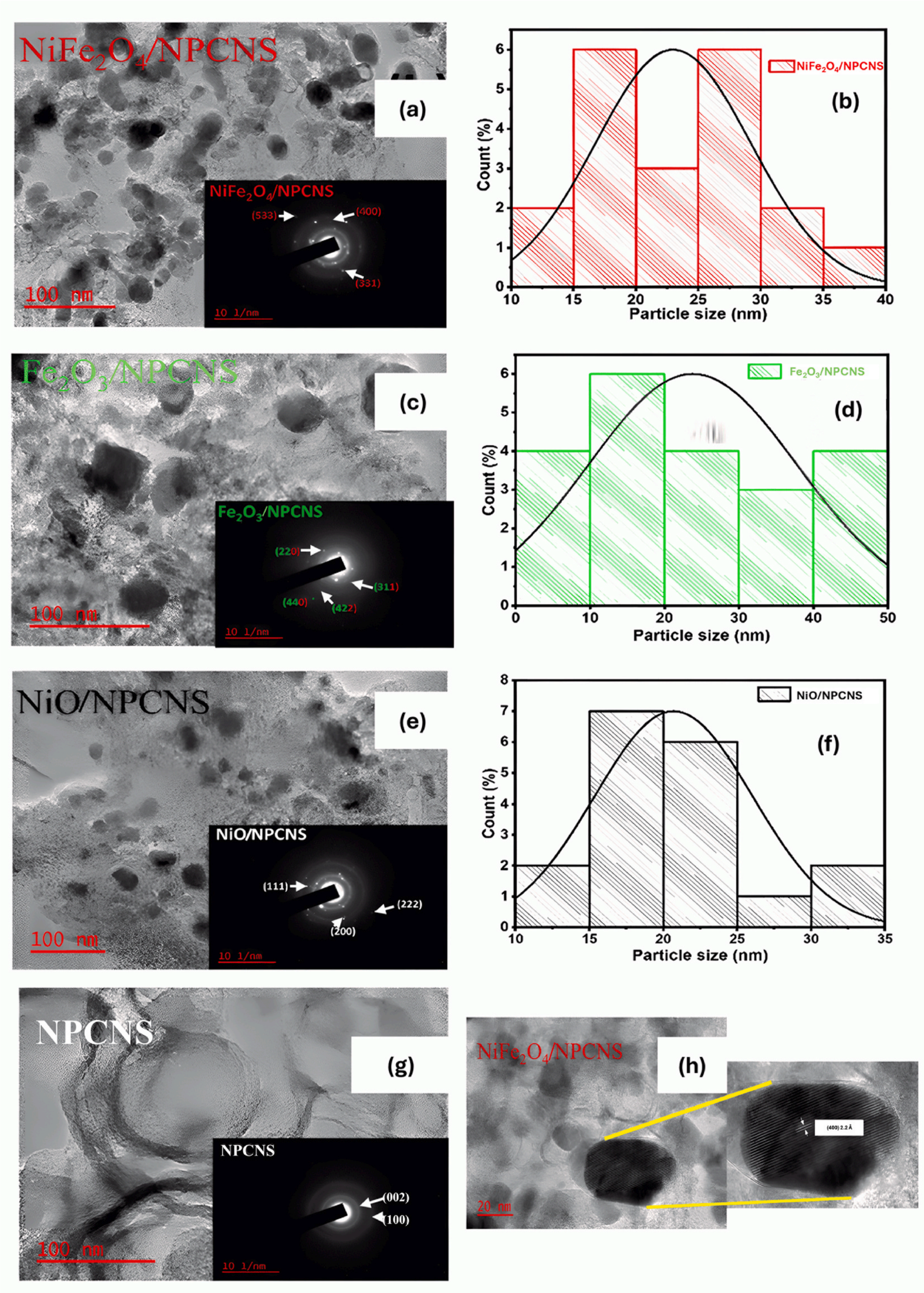

Fig. 3. TEM images for (a) $NiFe_2O_4$/NPCNS, (c) Fe_2O_3/NPCNS, (e) NiO/NPCNS, and (g) NPCNS with an inlet of SAED for all composites and histograms for particle size distribution on (b) $NiFe_2O_4$/NPCNS, (d) Fe_2O_3/NPCNS, and (f) NiO/NPCNS, and also the lattice fridge for the nanoparticles of $NiFe_2O_4$/NPCNS.

electrocatalytic activity.

Metal oxide hybrid nanocomposites have distinct morphologies compared to unsupported carbon. The NPCNS in Fig. 3(g) displayed multi-wrinkling, indicating secondary folding of carbon nanosheets after calcination, which is not observed in $NiFe_2O_4$/NPCNS, Fe_2O_3/NPCNS, and NiO/NPCNS. Metal oxides can prevent folding and expose more active sites, which is beneficial for electrocatalytic performance. Complex Spinel $NiFe_2O_4$ nanoparticles have a lattice fringe with a d-spacing of 2.2 Å (Fig. 3(h)), corresponding to the (400) miller index according to $NiFe_2O_4$ JCPDS No. 00-066-0245 and linked with XRD results of $NiFe_2O_4$/NPCNS. The particle size of nickel ferrite, iron (II) oxide, and nickel oxide on graphitic carbon nanosheets differs even when the same calcination temperature and heating rate are applied since those nanomaterials have different nucleation and growth kinetics.

The N_2 adsorption-desorption isotherm measurements were used to study the textural and porous properties of hybrid nanocomposites (Fig. 4(a)). All composites showed a mesoporous structure (volume defects that contribute to enhanced ORR), as evidenced by the classic type IV isotherm with a hysteresis loop between 0.5 and 1.0 of the relative pressure [25]. $NiFe_2O_4$/NPCNS had the highest BET specific surface area, total pore volume, and mean pore diameter compared to other nanomaterials. The findings are presented in Table S3.

$NiFe_2O_4$ nanoparticles were successfully grafted between NPCNS, resulting in an increase in surface area. $NiFe_2O_4$ formed on NPCNS formed a complex spinel $NiFe_2O_4$ which caused atoms to be displaced from their regular lattice positions creating point defects. This increases more active sites available for ORR, which leads to smoother ORR. The NPCNS structure prevents aggregation, resulting in a higher surface area. These findings are supported by Fig. 4(b)'s pore size distribution.

The study analyzed hybrid nanomaterials with mesoporous-dominated microstructure and pore diameters centered at 4 nm. $NiFe_2O_4$/NPCNS had more pore diameters between 4 and 120 nm, improving mass transport rates for ORR, while NPCNS had the lowest content of pore diameters between 20 and 120 nm due to secondary folding of carbon nanosheets, limiting the accessibility of active sites for ORR [26,27].

The Raman spectra of various nanomaterials are depicted in Fig. 4(c). The characteristic peaks of the carbon support are labeled with their respective vibration modes. The bending and stretching vibrations of the single tri-s-triazine unit are represented by Raman peaks centered around 490 cm^{-1} and 494 cm^{-1}, respectively [49]. Various types of s-triazine ring breathing modes are attributed to Raman peaks centered at 707 cm^{-1} and 980 cm^{-1}. Graphitic carbon nitride has strong RAMAN cross section which means that the strong RAMAN peaks between 490 cm^{-1} and 707 cm^{-1} overshadowed the weaker RAMAN signals from metals on $NiFe_2O_4$/NPCNS,

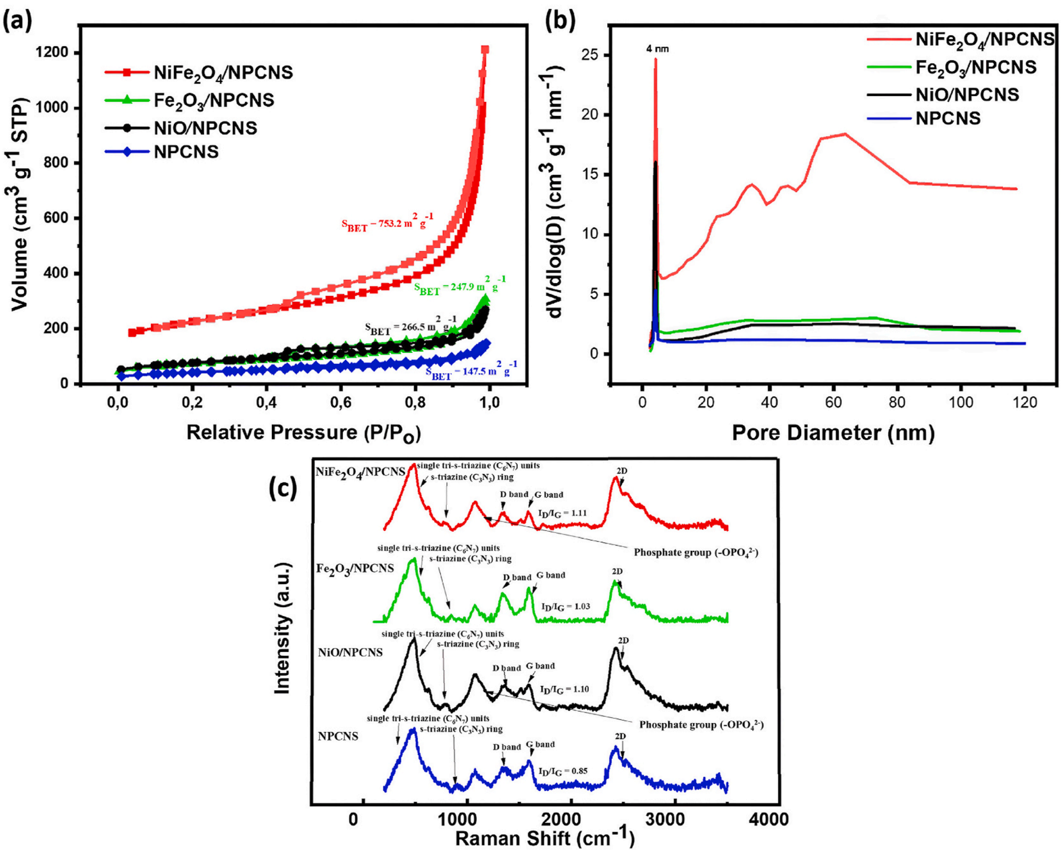

Fig. 4. (a) N_2 adsorption-desorption isotherms, (b) corresponding pore size distribution, and (c) RAMAN spectra of $NiFe_2O_4$/NPCNS, Fe_2O_3/NPCNS, NiO/NPCNS, and NPCNS hybrid nanomaterials.

Fe_2O_3/NPCNS, and NiO/NPCNS which explain why those peaks are less visible [65]. This means that the basic structure of the substrate material was not altered by intense heat treatments. Furthermore RAMAN peaks for metal-oxygen (M − O) bond are visible in high intensity from 200 cm^{-1} to 400 cm^{-1} which was not covered by our RAMAN analysis [66].

The presence of the 1100 cm^{-1} bands in all hybrid nanocomposites suggests the intercalated phosphate group (-OPO_4^{2-}) brought about by the lecithin used for phosphorus doping [50]. The increase in the intensity of the Raman peak at 1100 cm^{-1} can be linked to the creation of more vacancies on the carbon network due to the presence of heteroatoms like P, Fe, and Ni. This could explain why the intensity of the Raman peak at 1100 cm^{-1} for $NiFe_2O_4$/NPCNS is amplified.

In hybrid nanomaterials, two peaks resembling graphitized lamellar structure are identified as the D band (1338-1368 cm^{-1}) and the G band (1584-1595 cm^{-1}) [28]. The D band signifies lattice defects induced by heteroatom doping, while the G band represents in-plane stretching vibration of sp^2-hybridized carbon [29]. The presence of the 2D band at 2422 cm^{-1} indicates a higher degree of graphitization in all nanocomposites. The intensity ratio (I_D/I_G) shown in Fig. 4 and Table S4, suggests structural disorder, with $NiFe_2O_4$/NPCNS exhibiting the highest ratio, indicating a less sequential graphene-like structure since a long range order of graphene like structures are heavily disrupted by defects.

The X-ray photoelectron spectroscopy was used to characterize the surface chemical composition and oxidation states of $NiFe_2O_4$/NPCNS, Fe_2O_3/NPCNS, and NiO/NPCNS. The survey spectra showed prominent peaks for C 1s, O 1s, N 1s, Fe 2p, Ni 2p, and P 2p in $NiFe_2O_4$/NPCNS, C 1s, O 1s, N 1s, Fe 2p, and P 2p in Fe_2O_3/NPCNS, and C 1s, O 1s, N 1s, Ni 2p, and P 2p in NiO/NPCNS.

The high-resolution spectra for C 1s (Fig. 5(a)) after deconvolution depicted four peaks centered at 284.0, 285.2, 286.4, and 288.9 eV for $NiFe_2O_4$/NPCNS, 284.9, 286.1, 287.5, and 289.0 eV for Fe_2O_3/NPCNS, and 284.6, 285.9, 287.7, and 289.7 eV for NiO/NPCNS corresponding to sp^2-C, sp^3-C, C–N/C–P, and C=O configurations [30,31]. The successful co-doping with nitrogen and phosphorus was confirmed by the presence of C–N/C–P bonds. The dominant carbon environment on the carbon matrix was the sp^2 hybridized carbon as evident by the high intensity of the peaks at 284.0, 284.9, and 284.6 eV for $NiFe_2O_4$/NPCNS, Fe_2O_3/NPCNS, and NiO/NPCNS, which was consistent with the RAMAN spectra. The peaks at 288.9, 289.0, and 289.7 eV for the C=O bond on $NiFe_2O_4$/NPCNS, Fe_2O_3/NPCNS, and NiO/NPCNS are mainly located at the edge of the NPCNS as oxygen defects.

The high-resolution spectra for N 1s (Fig. 5(b)) showed six prominent peaks for the nitrogen species centered at 397.3, 398.4, 399.2, 400.5, 401.3, and 405.3 eV for $NiFe_2O_4$/NPCNS, 398.0, 398.9, 399.9, 401.4, 402.8, 405.4 eV for Fe_2O_3/NPCNS, and 397.9, 399.0, 399.8, 400.8, 402.3, and 404.7 eV for NiO/NPCNS which were attributed to pyridinic N, metal-N, hydrogenated-N (N–H, which includes pyrrolic N and hydrogenated pyridine), graphitic N, bulk N–H, and oxidized N, respectively [32,33,67]. The highly active graphitic N on $NiFe_2O_4$/NPCNS has the highest relative content, which is beneficial for the catalytic activity of the hybrid nanocomposite. Pyridinic N, and graphitic N configurations as substitutional defects have been proven to be fundamental ORR active sites for nitrogen-doped carbon nanocomposites by tuning the charge distribution of the carbon matrix to favour the $4e^-$ transfer process. Fe/Ni–N configuration on the N 1s spectrum also contributes to the exceptional electrocatalytic activity of $NiFe_2O_4$ NPCNS [21].

The O 1s high resolution spectra shown in Fig. 5(c) showed four prominent peaks for the oxygen species centered at 529.8, 530.8, 531.8, and 532.7 eV for $NiFe_2O_4$/NPCNS, 530.3, 531.3, 532.3, and 533.5 eV for Fe_2O_3/NPCNS and 530.6, 531.8, 533.2, and 534.3 eV

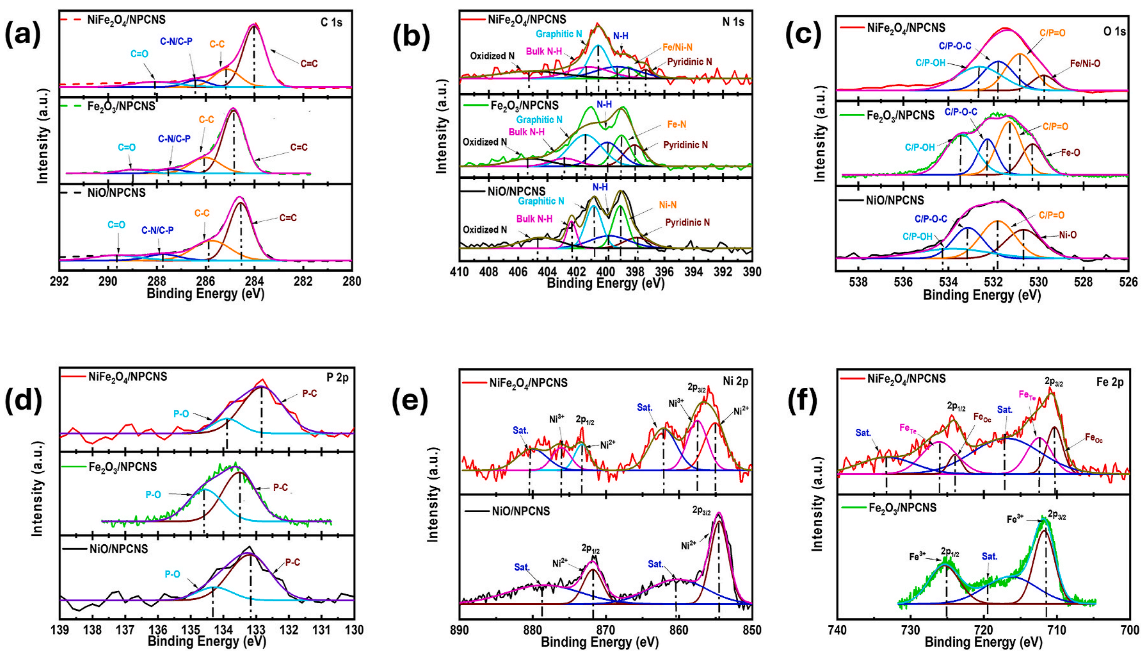

Fig. 5. XPS spectra after deconvolution for $NiFe_2O_4$/NPCNS, Fe_2O_3/NPCNS, and NiO/NPCNS (a) C 1s spectra, (b) N 1s spectra, (c) O 1s spectra, (d) P 2p spectra, (e) Ni 2p spectra and, (e) Fe 2p spectra.

for NiO/NPCNS, corresponding to Metal-O, C/P=O, C/P–O–C, and C/P–OH, respectively. The C/P=O and C/P–O bonds had the highest relative content and acted as oxygen defects at the edge of the NPCNS lattice [4,34].

The P 2p high resolution spectra shown in Fig. 5(d) depicts two distinctive peaks centered at 132.8 and 134.9 eV for $NiFe_2O_4$/NPCNS, 133.5 and 134.6 eV for Fe_2O_3/NPCNS, and 133.1 and 134.3 eV for NiO/NPCNS, which correspond to the P–C and P–O bonds on the carbon lattice [35]. The relatively high P–C bond proportion in the hybrid nanomaterials shows the chemical bonding of phosphorus into the carbon framework. The high P–C content of $NiFe_2O_4$/NPCNS enhances its electrocatalytic activity for ORR by providing surface-active phosphorus sites as substitutional defects. The energy difference between each component of C 1s, N 1s, O 1s, and P 2p remains consistent, but the overall relative binding energies for the spectra of Fe_2O_3/NPCNS and NiO/NPCNS shifts to higher values, making the systems insulating. This explains why $NiFe_2O_4$/NPCNS has higher ORR electrocatalytic activity than both Fe_2O_3/NPCNS and NiO/NPCNS.

The deconvolution of the Ni 2p spectra in Fig. 5(e) shows six definitive peaks centered at 855.1, 857.5, 862.2, 873.3, 876.2, and 880.3 eV for $NiFe_2O_4$/NPCNS and four prominent peaks centered at 854.6, 860.5, 871.8, and 878.0 eV for NiO/NPCNS. The peaks are caused by spin-coupling with the satellite peaks and the two-shake-up type peaks for Ni at high binding energy side of the Ni $2p_{3/2}$ and Ni 2 $p_{1/2}$ edge. The two main peaks (Ni $2p_{3/2}$ and $2p_{1/2}$) demonstrated the presence of Ni^{2+} and Ni^{3+} cations for $NiFe_2O_4$/NPCNS and only Ni^{2+} cations for NiO/NPCNS [36]. The two peaks at 857.5 and 876.2 eV for $NiFe_2O_4$/NPCNS belong to Ni^{3+}, which was caused by

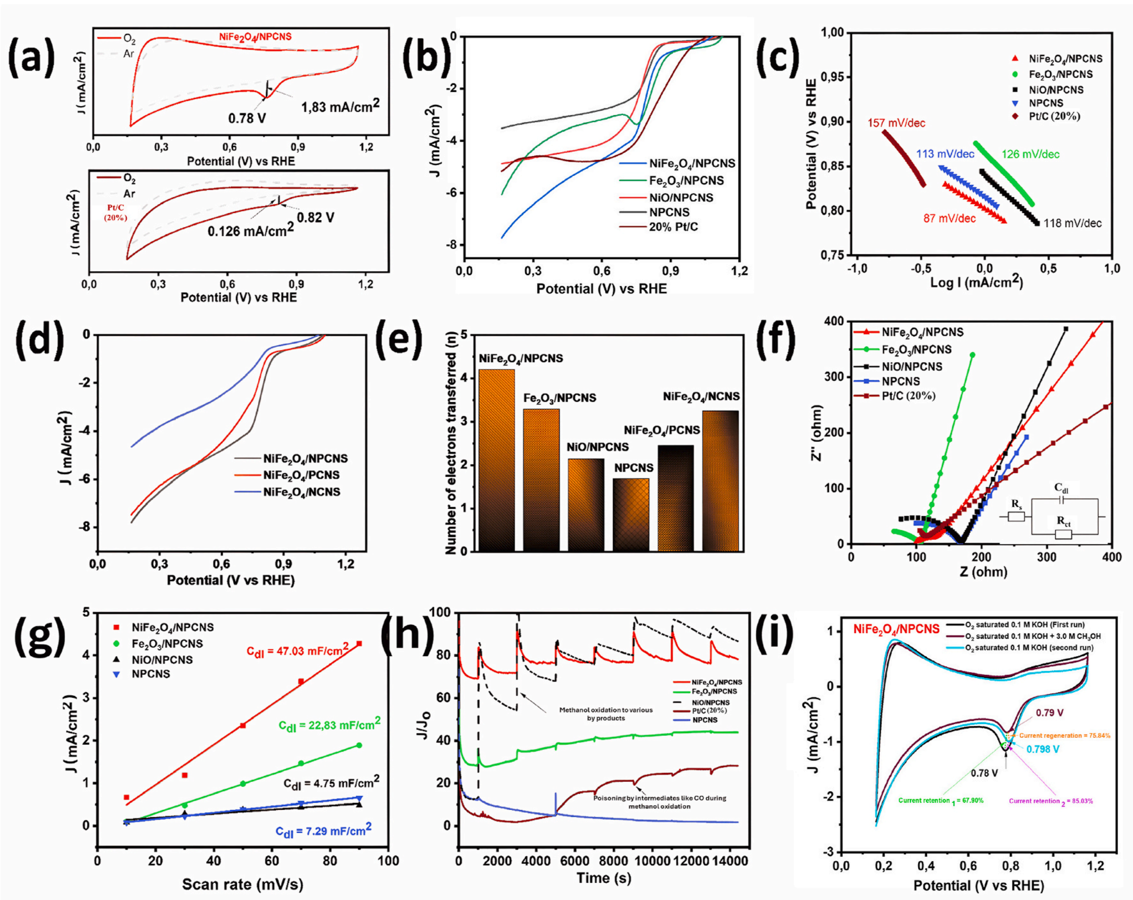

Fig. 6. (a) Cyclic Voltammetry (CV) curves towards ORR on the synthesized $NiFe_2O_4$/NPCNS, and 20 % Pt/C in an O_2-saturated and Ar-saturated 0.1M KOH solution, (b) Linear sweep voltammetry (LSV) curves of the synthesized $NiFe_2O_4$/NPCNS, Fe_2O_3/NPCNS, NiO/NPCNS, NPCNS, and an inlet of the commercial 20 % Pt/C at 1600 rpm and a scan rate:10 mV/s, (c) Tafel slopes of all electrocatalysts in O_2 saturated 0.1M KOH solution at 1600 rpm and a scan rate of 10 mv s^{-1}, (d, e) Linear sweep voltammetry (LSV) curves of the synthesized $NiFe_2O_4$/NPCNS, $NiFe_2O_4$/PCNS, and $NiFe_2O_4$/NCNS at 1600 rpm and a scan rate:10 mV/s, and the number of electrons transferred during ORR for all hybrid electrocatalysts, (f) A Nyquist plots for all metal oxide hybrid electrocatalysts including the commercial 20 % Pt/C measured at a potential of 0.29 V and a frequency range of 100 kHz–0.5 Hz, (g) Double layer capacitance obtained from cyclic voltammetric (CV) curves in the non-faradaic region at various scan rates of 10, 30, 50, 70, 90 mV/s in argon saturated 0.1 M KOH electrolyte solution and corresponding capacitive current at 1.06 V against the scan rate for the CV tests, (h) Current–time responses of the synthesized hybrid nanomaterials and commercial 20 % Pt/C in O_2 saturated 0.1 M KOH at 0.45 V upon continuous addition of 3.0 M methanol in increments to the electrolyte solution at 1000 s, 3000 s, 5000 s, 7000 s, 9000 s, 11 000 s, and 13 000 s respectively, and (i) Cyclic voltammetry (CV) responses for $NiFe_2O_4$/NPCNS in O_2 saturated 0.1 M KOH electrolyte before and after adding 3.0 M methanol to evaluate the effect of methanol on the ORR.

the partial surface oxidation of the nickel on $NiFe_2O_4$ at high temperatures as it transitioned from an inverse spinel structure to a complex spinel structure [68].There was an up-shift of ca. 1.4 eV for Ni $2p_{3/2}$ and 1.7 eV for Ni $2p_{1/2}$ at the binding energy of the peaks for $NiFe_2O_4$/NPCNS in comparison to NiO/NPCNS. This increase in the binding energy for the Ni 2p peaks was attributed to the strong attachment of the $NiFe_2O_4$ nanoparticles to the NPCNS via Ni–N and Ni–O–C bonds during hybridization.

The Fe 2p core level spectra in Fig. 5(f) for Fe species on $NiFe_2O_4$/NPCNS indicates successful formation of a $NiFe_2O_4$ complex spinel structure. Deconvolution reveals that the Fe species exist in more than one coordination environment as Fe^{2+} and Fe^{3+} species exist in both the octahedral and tetrahedral sites [69]. Peaks at 710.2 and 712.4 eV are assigned to Fe octahedral (B site) and Fe tetrahedral (A site) for Fe $2p_{3/2}$, while peaks at 723.9 and 725.8 eV correspond to Fe octahedral (B site) and Fe tetrahedral (A site) for Fe $2p_{1/2}$ [37]. The widely dispersed nanoparticles on $NiFe_2O_4$/NPCNS contribute to a high content of Ni^{2+}, Ni^{3+}, Fe^{2+}, and Fe^{3+} species which is consistent with their occupation of different lattice sites, and which is indicative of the increased active sites for enhanced ORR electrocatalytic activity. The Fe 2p core level spectra after deconvolution for Fe_2O_3/NPCNS revealed two distinct peaks located at 711.5 and 725.0 eV corresponding to Fe $2p_{3/2}$ and Fe $2p_{1/2}$ which can be used to qualitatively determine the ionic state of iron on the composite. In addition to the appearance of these two peaks, a satellite peak at 719.6 eV was observed which was consistent with the characterization of Fe^{3+} [21].

3.2. *Electrocatalytic oxygen reduction and CO-tolerance studies*

The electrocatalytic activity of hybrid electrocatalysts and commercial 20 % Pt/C was assessed using a three-electrode system. A linear correlation between cathodic peak current and scan rates (Fig. S4) indicated that the electroactive oxygen species in this diffusion-limited process were confined on the modified rotating disk electrode (RDE) surface [38]. The cathodic peak current densities shifted negatively with increasing scan rate, suggesting enhanced oxygen reduction capability. The results imply diffusion-limited ORR processes across all hybrid electrocatalysts. As shown in Fig. 6(a) and Fig. S5, quasi-rectangular cyclic voltammetry (CV) curves were observed for all electrocatalysts in Ar-saturated 0.1 M KOH electrolyte solution, with no distinctive cathodic peak in the potential range of 0.0–1.2 V vs. RHE. Conversely, in oxygen-saturated 0.1 M KOH electrolyte solution, all hybrid electrocatalysts, including 20 % Pt/C, displayed CV curves with respective cathodic peaks.

Analyzing the cathodic peak potential revealed a positive shift in the following order: Fe_2O_3/NPCNS (0.79 V vs. RHE), $NiFe_2O_4$/NPCNS (0.78 V vs. RHE), NPCNS (0.77 V vs. RHE), and NiO/NPCNS (0.66 V vs. RHE). The cyclic voltammetry curves indicated an increasing ORR activity trend as follows: NiO/NPCNS < NPCNS < $NiFe_2O_4$/NPCNS < Fe_2O_3/NPCNS. The net peak current density (NPCD) for $NiFe_2O_4$/NPCNS, calculated by subtracting the background current from the cathodic peak current, was the highest among the hybrid electrocatalysts, indicating superior ORR electrocatalytic activity. Specifically, the NPCD for $NiFe_2O_4$/NPCNS reached 1.83 mA/cm^2, twice as high as that of the commercial 20 % Pt/C (0.126 mA/cm^2) according to Fig. 6(a).

The electrocatalytic activity of hybrid electrocatalysts, particularly $NiFe_2O_4$/NPCNS, was assessed and compared with commercial 20 % Pt/C using linear sweep voltammetry at 1600 rpm in an O_2-saturated 0.1 M KOH electrolyte solution. $NiFe_2O_4$/NPCNS exhibited notable performance, with an onset potential (0.92 V vs. RHE) close to 20 % Pt/C (0.97 V vs. RHE) and a current density at 0.164 V (−7.81 mA/cm^2) surpassing that of 20 % Pt/C as shown in Fig. 6(b). Notably, $NiFe_2O_4$/NPCNS displayed the lowest Tafel slope (87 mV/dec) as shown in Fig. 6(c), indicating a high exchange current density of interfaces between the catalyst and the electrode [4]. This highlights the superior electrocatalytic activity of $NiFe_2O_4$/NPCNS for ORR compared to other nanomaterials in the study, including Fe_2O_3/NPCNS, NiO/NPCNS, and NPCNS.

Linear sweep voltammetry was conducted at a rotation speed of 1600 rpm in an O_2-saturated 0.1 M KOH electrolyte solution for $NiFe_2O_4$/NPCNS, $NiFe_2O_4$/PCNS, and $NiFe_2O_4$/NCNS to explore the impact of nitrogen and phosphorus co-doping on carbon nanosheets. As seen in Fig. 6(d) and Table S5, $NiFe_2O_4$/NPCNS exhibited the highest onset, half-wave, and current density compared to $NiFe_2O_4$/PCNS and $NiFe_2O_4$/NCNS, suggesting a synergistic electrocatalytic enhancement from co-doping. Additionally, a secondary onset potential observed for phosphorus mono-doped carbon nanosheets on the $NiFe_2O_4$/PCNS nanocomposite indicated a mixture of 2 e^- and 4 e^- transfer pathways.

A catalyst exhibiting a high current density with a combination of two- and four-electron processes for oxygen reduction reaction can reduce oxygen to water. However, preference for the two-electron process, leading to hydrogen peroxide production, can impact fuel cell performance negatively. $NiFe_2O_4$/NCNS, despite favoring a 4 e^- process with ∼3.25 electrons transferred, exhibits low current density as shown in Fig. 6(e) and Table S5. In contrast, $NiFe_2O_4$/NPCNS, mainly following a 4 e^- process, proves to be the superior electrocatalyst, displaying both high current density and effective oxygen-to-water conversion at a superior rate compared to $NiFe_2O_4$/NCNS and $NiFe_2O_4$/PCNS.

The electron transferred (n) for Fe_2O_3/NPCNS falls within the 2–4 range (∼3.28), significantly higher than NiO NPCNS (∼2.13) and NPCNS (∼1.68)) according to Fig. 6(e) and Fig. S6. This points to a two-electron process for NiO/NPCNS and NPCNS, resulting in more H_2O_2 production rather than water during ORR. The presence of gamma iron (II) oxide nanoparticles on NPCNS enhances conductivity at low potential due to Fe–N active sites. Also, the high surface area of gamma-Fe_2O_3 and complex spinel $NiFe_2O_4$ nanoparticles on Fe_2O_3/NPCNS and $NiFe_2O_4$/NPCNS provides more active sites for ORR, therefore as the ORR progresses, more oxygen molecules are adsorbed onto the active sites which facilitates the reduction process and increases the current density. This explains why the current density on those composites has a tendency to increase. $NiFe_2O_4$/NPCNS outperforms monometallic oxide nanohybrids in ORR, thanks to higher conductivity and active sites such as Ni–N–C, Fe–N–C, C–P, and C–N (graphitic N and pyridinic N). Comparative analysis in Table S6 suggests that $NiFe_2O_4$/NPCNS excels among reported electrocatalysts due to the NPCNS pore structure, facilitating greater mass transfer and exposing more active sites (C–P, C–N, metal-N) for O_2 reduction [63,70–73].

Polarization curves were generated using a Rotating Disk Electrode (RDE) with varying rotation speeds (400 rpm–2500 rpm) in an

O_2-saturated 0.1 M KOH electrolyte solution at a scan rate of 10 mV/s. The results, depicted in Figs. S6, S7, and S8, illustrate increased current density with higher rotation speeds, indicating improved electrolyte ion transit. ORR kinetics were further examined through Koutecky-Levich plots (K-L plots) at different potentials (0.2 V–0.6 V vs. RHE), demonstrating strong linearity for O_2 reduction within that potential range [39]. The number of electrons transferred (n) per O_2 at various potentials were calculated using the K-L equation, as depicted in Figs. S6, S7, and S8.

The polarization curves for $NiFe_2O_4$/NPCNS in Fig. S8 show a minimal potential change of only 14 mV from 400 to 2500 rpm at 3.0 mA cm^2. This shift is attributed to concentration polarization, signifying reactant (O_2 in electrolyte) depletion at the electrode surface. As the catalyst is fully utilized, the potential difference between the electrode surface and electrolyte decreases, indicating efficient reactant consumption at the catalyst surface. Additionally, the presence of different metal ions (Ni^{2+}, Ni^{3+}, Fe^{2+}, and Fe^{3+}) and oxygen vacancies (caused by elevated temperatures) can influence the electronic structure during ORR, causing shifts in redox potentials, though without affecting the onset potential.

The electrocatalytic performance of a catalyst in the ORR is closely linked to its low charge transfer resistance, a parameter determined through electrochemical impedance spectroscopy (EIS) [32]. By analyzing Nyquist plots and fitting them, both solution resistance and charge transfer resistance of cathode electrocatalysts were identified (Table S7). EIS measurements at an open circuit were conducted for nanohybrid electrocatalysts and commercial 20 % Pt/C, spanning a frequency range from 100 KHz to 0.5 Hz at a potential of 0.29 V. The semicircles observed in the high-frequency range represent the metal oxide hybrid electrocatalysts and 20 % Pt/C, with the real axis intercepts used to estimate electrolyte resistance (R_s) and charge transfer resistance (R_{ct}). It was observed that the R_{ct} of all electrocatalysts decreased in the following order: NiO/NPCNS > NPCNS > Fe_2O_3/NPCNS >20 % Pt/C > $NiFe_2O_4$/NPCNS as depicted in Fig. 6(f).

The introduction of nitrogen and phosphorus atoms to carbon nanosheets enhances charge transfer kinetics, leading to lower charge transfer resistance compared to commercial 20 % Pt/C. The addition of gamma iron oxide to the N, P-co-doped carbon support further improves charge transfer kinetics, with Fe_2O_3/NPCNS exhibiting lower resistance than NiO/NPCNS and NPCNS. $NiFe_2O_4$/NPCNS demonstrates the lowest charge transfer resistance due to enhanced bonding at the interface of active sites, accelerating ORR kinetics [40].

The density of electrochemically active sites in all hybrid electrocatalysts was determined through electrochemically active surface area (EASA) calculation, associated with double layer capacitance (C_{dl}) in the non-faradaic region (Fig. 6(g) and Fig. S9) [41]. $NiFe_2O_4$/NPCNS showed the highest C_{dl}, indicating superior exposure of active sites and facilitating efficient O_2 reduction. This excellent electrochemical performance is attributed to synergistic effects and electronic contributions between the multi-metal oxide and co-doped carbon nanosheets, resulting in a porous conductive network nanohybrid structure with increased EASA, enhanced electron transport ability, and effective mass transport between adsorbed oxygen molecules on active sites.

The potential methanol crossover effect is crucial for the practical use of catalysts in fuel cells. The electrocatalytic selectivity of all hybrid electrocatalysts, including commercial 20 % Pt/C, was examined through chronoamperometry at 0.45 V vs. RHE in O_2-saturated 0.1 M KOH with the presence of methanol. Fig. 6(h) indicates that gamma Fe_2O_3 nanoparticles on Fe_2O_3/NPCNS can oxidize methanol, resulting in a sharp current increase upon methanol addition to the electrolyte. In an alkaline electrolyte, OH^- anions adsorb on the catalysts to form Fe_2O_3-OH_{ads} species, which then react with CH_3OH_{ads} to produce CH_2OH intermediate and H_2O as a by-product as depicted in equations 1 and 2 on SI [42].

The decline and subsequent increase in current observed after adding methanol at 1000 s indicate the re-establishment of a conductive path, leading to active site regeneration. Electro-oxidation of CH_2OH by-product and CH_3OH at 3000 s, following the addition of 1 mL of 3.0 M methanol, shows a sharp increase in current, followed by a gradual decrease and a steady increase again. This pattern signifies the formation of a conductive path between the electrode and the electrolyte, facilitating the flow of electrons.

The addition of 1 mL of 3.0 M methanol at 5000 s results in a sharp decrease in current, indicating inhibition of methanol oxidation and subsequent poisoning on Fe_2O_3/NPCNS. This is attributed to the accumulation of CO on the active sites and catalyst surface. Continuous formation of Fe_2O_3-OH_{ads} species helps oxidize the poisonous CO-like species, freeing up active sites [61]. The peak intensity for poisoning decreases with incremental additions of 1 mL of 3.0 M methanol at 7000 s, 9000 s, 11 000 s, and 13 000 s, accompanied by slight methanol oxidation. After 9000 s, a stable diffusion-limited region is reached, and the catalyst remains stable even in the presence of methanol.

NiO nanoparticles on NiO/NPCNS undergo oxidation to $Ni(OH)_2$ in the presence of OH^- in an alkaline medium (equation 3 on SI). The resulting modifier layer, $Ni(OH)_2$, acts as the electrocatalyst for methanol oxidation [43]. Upon adding methanol after 1000 s, the electroactive species (NiOOH) generated from $Ni(OH)_2$ oxidation (equation 4 on SI) react with methanol, leading to CH_2OH production and a sharp increase in current, as observed in Fig. 6(h). Additionally, $Ni(OH)_2$ is generated (equation 5 on SI), allowing for further methanol oxidation and correlating with the steepest increase in current upon methanol addition, as shown in Fig. 6(h).

NiO nanoparticles on NiO/NPCNS can undergo direct oxidation to produce NiOOH (equation 6 on SI), and the adsorbed NiOOH can directly react with methanol to form an intermediate product. This imparts high stability to NiO/NPCNS when methanol is introduced in further increments at 3000s, 5000s, 7000s, 9000s, 11000s, and 13000s. This results in further methanol oxidation, a sharp increase in current, and notably, no sharp decline in current due to CO poisoning.

The chronoamperometric response test for commercial 20 % Pt/C reveals methanol oxidation peaks upon adding 1 mL of 3.0 M methanol at 1000 s. Despite the Pt catalyst's ability to oxidize methanol and its intermediates at low methanol concentrations, its low CO tolerance is evident. No further methanol oxidation is observed at 3000 s and 5000 s, but a gradual increase in current is established. Initially, the current response decreases due to CO adsorption on the catalyst surface, blocking active sites and slowing the electrochemical reaction. However, with continued low concentration CO exposure, the current response gradually rises, indicating CO oxidation on the catalyst surface and providing additional active sites for the electrochemical reaction.

Inhibition due to CO poisoning is observed with a sharp decrease in current upon adding methanol at 7000 s, 9000 s, 11 000 s, and 13 000 s, indicating that CO accumulation has blocked all active sites on Pt. The increase in CO concentration forms Pt-CO_{ads} on the Pt catalyst surface, inhibiting further methanol electro-oxidation [42]. In contrast, NPCNS shows methanol oxidation peaks at 1000 s and 5000 s in an O_2 saturated KOH solution, attributed to OH^- species on its surface. NPCNS demonstrates better methanol tolerance, as no CO poisoning is observed upon adding 1 mL of 3.0 M methanol at 3000 s, 7000 s, 9000 s, 11 000 s, and 13 000 s.

The primary drawback of NPCNS is its low current retention in the presence of methanol compared to other hybrid electrocatalysts. However, $NiFe_2O_4$/NPCNS, featuring both Fe_2O_3-OH_{ads} and $Ni(OH)_{2ads}$ and/or $NiOOH_{ads}$ active sites for methanol oxidation and more actives sites due to the complex spinel structure, exhibits the best current retention when methanol is introduced incrementally after 1000s, 3000s, 7000s, 9000s, 11000s, and 13000s. This characteristic is advantageous for fuel cell commercialization. Consequently, $NiFe_2O_4$/NPCNS, along with NiO/NPCNS and Fe_2O_3/NPCNS, demonstrates superior methanol tolerance compared to commercial 20 % Pt/C and, subsequently, better ORR selectivity.

The electrochemical properties of all hybrid electrocatalysts and commercial Pt/C in the presence of methanol were assessed using cyclic voltammetry, illustrated in Fig. 6(i) and Fig. S10. Non-noble metal electrocatalysts like Fe–N/C were reported to have unstable metal ions and redox couples within specific electrochemical windows [44,45]. However, hybrid electrocatalysts in this study with mono- or multi-metal oxides showed no redox couples due to metal oxide introduction, indicating their chemical and electrochemical stability in the presence of methanol.

All hybrid electrocatalysts maintained higher selectivity for ORR even after the introduction of methanol, while Pt/C exhibited significantly reduced ORR and emphasized its high selectivity towards methanol oxidation. Considering that many efficient Pt-based ORR catalysts also catalyze methanol oxidation, there is a demand for ORR catalysts with high methanol tolerance for fuel cell commercialization. The hybrid electrocatalysts demonstrated a positive shift in cathodic peak potential in response to methanol addition, as depicted in Fig. 6(i) and Fig. S10. Current $retention_1$, calculated using cathodic peak current density before and after methanol addition, served as a metric to evaluate the selectivity of an electrocatalyst towards ORR and/or methanol oxidation.

$NiFe_2O_4$/NPCNS exhibited the highest current $retention_1$ of 67.90 % compared to mono-metal oxides on NPCNS, indicating its superior selectivity for ORR. In contrast, NiO/NPCNS showed the lowest current $retention_1$ of 55.85 % among all nanohybrid electrocatalysts, supporting its effectiveness for methanol oxidation and suggesting a balanced response to methanol oxidation and ORR. NPCNS demonstrated a current $retention_1$ of 80.97 % and displayed higher selectivity for ORR, suggesting that the co-doped carbon support was relatively inactive towards methanol oxidation, with hydroxide ions on its surface facilitating methanol oxidation.

The current regeneration for all electrocatalysts, calculated by comparing cathodic peak current density after methanol addition with that obtained in post-methanol cyclic voltammetry, was employed to assess active site regeneration for oxygen reduction. $NiFe_2O_4$/NPCNS demonstrated the highest current regeneration at 75.84 % among mono-metal oxides nanohybrid electrocatalysts, indicating superior regeneration of active sites for ORR and benefiting fuel cell commercialization. NPCNS exhibited a current

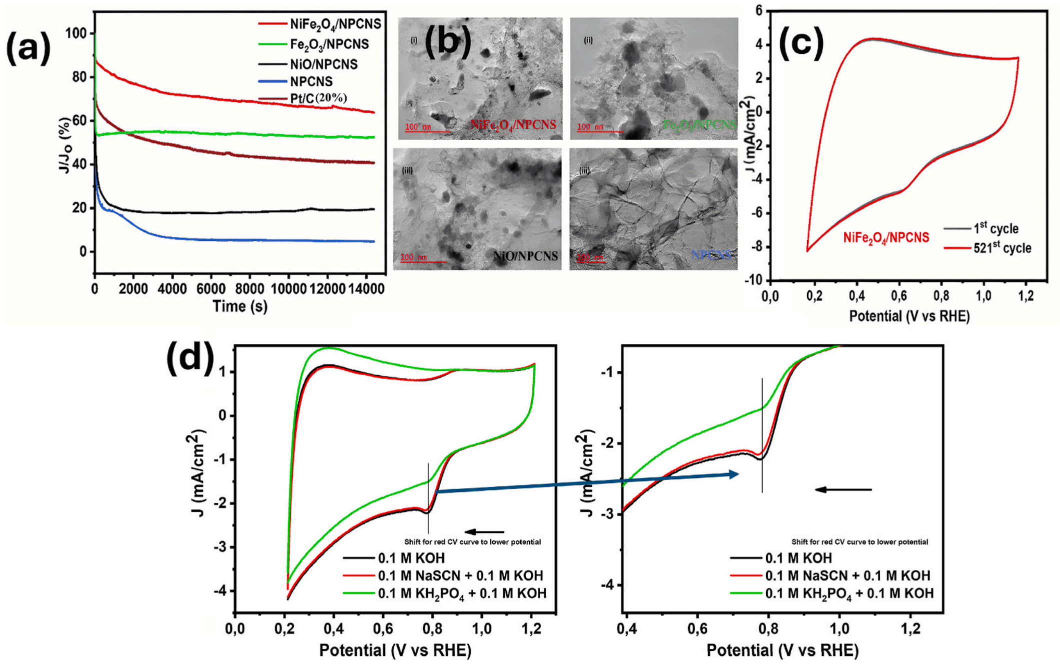

Fig. 7. (a) Stability test results of the synthesized hybrid nanomaterials and commercial Pt/C under continuous O_2 reduction at 0.45 V vs. RHE for 4 h, (b) TEM images of $NiFe_2O_4$/NPCNS, Fe_2O_3/NPCNS, NiO/NPCNS, and NPCNS nanomaterials obtained after electrochemical measurements, (c) Durability studies for $NiFe_2O_4$/NPCNS in O_2 saturated 0.1 M KOH at 100 mV/s, and (d) Cyclic voltammetry curves of $NiFe_2O_4$/NPCNS nanocomposite used to study the active sites present on the hybrid electrocatalyst.

regeneration of 85.14 %, suggesting the regeneration of hydroxide groups functionalized on the carbon nanosheets' surface and utilized in ORR.

Current $retention_2$, calculated by comparing initial cathodic peak current density before methanol addition with that after methanol addition, served as another measure of active site regeneration. $NiFe_2O_4$/NPCNS, NiO/NPCNS, and NPCNS exhibited the highest current $retention_2$, indicating minimal to no CO poisoning on these electrocatalysts, as suggested in Fig. 6(i) and Fig. S10. In contrast, Fe_2O_3/NPCNS had the lowest current $retention_2$, implying some active sites on that catalyst were blocked by CO due to methanol addition.

3.3. Stability, durability and active site poisoning for oxygen reduction reaction studies

The stability of catalysts is crucial for practical use in fuel cells. Chronoamperometric analysis at 0.45 V vs. RHE in an O_2-saturated 0.1 M KOH electrolyte solution was conducted for various hybrid electrocatalysts, comparing them to commercial 20 % Pt/C. $NiFe_2O_4$/NPCNS demonstrated superior stability, maintaining the highest current retention after 4 h compared to 20 % Pt/C and other catalysts. This stability was attributed to favorable metal support interactions between $NiFe_2O_4$ nanoparticles and the graphene-like carbon support. Additionally, $NiFe_2O_4$/NPCNS exhibited the lowest H_2O_2 poisoning, evident by minimal current degradation over time.

NiO/NPCNS and NPCNS exhibited a pronounced decline in J/Jo (%) over time, likely due to H_2O_2 poisoning on their surfaces during O_2 reduction, following a two-electron process. Transmission electron microscopy (TEM) images in Fig. 7(b) and S11 from a Rotating Disk Electrode (RDE) after electrochemical analysis showed consistent particle size distributions for $NiFe_2O_4$/NPCNS, Fe_2O_3/NPCNS, NiO/NPCNS, and NPCNS. These distributions were comparable to those obtained before electrochemical analysis (Fig. 3), indicating high physicochemical and electrochemical stability in these nanocomposites.

The durability of $NiFe_2O_4$/NPCNS was assessed through cyclic voltammetry, subjecting it to potential between 0.164 and 1.164 V vs. RHE in an O_2-saturated 0.1 M KOH electrolyte at room temperature. After 521 cycles, the cyclic voltammograms exhibited no significant changes, indicating minimal loss of active surface area over 2 h (Fig. 7(c)). The high durability is attributed to strong covalent bonds between active sites and the graphitic carbon lattice [46]. Additionally, Fig. S12 provides a detailed molecular orbital theory explanation of the ORR for $NiFe_2O_4$/NPCNS [74–77].

Thiocyanate ions (SCN^-), known for selectively poisoning metal catalysts, were introduced to the electrolyte solution in $NiFe_2O_4$/NPCNS, $NiFe_2O_4$/PCNS, and $NiFe_2O_4$/NCNS to assess the impact of metal oxide incorporation on the ORR [51,52]. Upon adding 2 mL of 0.1 M NaSCN to 50 mL of 0.1 M KOH electrolyte solution, a shift in the cathodic peak potential for $NiFe_2O_4$/NPCNS and $NiFe_2O_4$/PCNS towards lower potentials and reduced current density suggested decreased ORR activity due to some metal active sites being blocked by SCN^- ions. However, the ORR activity did not completely vanish. See Fig. 7(d) and Fig. S13 for visual representations.

In 0.1 M KOH with 0.1 M NaSCN, $NiFe_2O_4$/PCNS exhibited a more pronounced reduction in current density than $NiFe_2O_4$/NPCNS and $NiFe_2O_4$/NCNS, as seen in CV curves. Ni-pyridinic N–C, Fe-pyridinic N–C, Ni-graphitic N–C, and Fe–N-graphitic N–C bonds at the active site interfaces in $NiFe_2O_4$/NPCNS and $NiFe_2O_4$/NCNS accelerate ORR kinetics, minimizing current density loss even when some active sites are poisoned by SCN^- ions. This contrasts with $NiFe_2O_4$/PCNS, lacking these active sites, resulting in a greater reduction in current density. This suggests that, while complex spinel nickel ferrite is active in $NiFe_2O_4$/NPCNS during ORR, additional active centers are present in this hybrid nanocomposite.

The impact of mono-doped or co-doped carbon nanosheets on the ORR activity of $NiFe_2O_4$/NPCNS, $NiFe_2O_4$/PCNS, and $NiFe_2O_4$/NCNS was investigated by adding KH_2PO_4 to the electrolyte solution and conducting CV curves (Fig. 7(d)). Given carbon's higher affinity for PO_4^{3-} compared to OH^- ions, the presence of PO_4^{3-} in the electrolyte hinders the interaction between carbon nanosheets and OH^-, consequently reducing the contribution of the nanocomposite's carbon nanosheets to the overall ORR activity [53].

The co-doped carbon nanosheets significantly contributed to the ORR activity, evidenced by a notable high reduction in current density in $NiFe_2O_4$/NPCNS upon adding 2 mL of 0.1 M KH_2PO_4 to a 0.1 M KOH electrolyte solution (Fig. 7(d)). The synergy between complex spinel nickel ferrite active sites and co-doped carbon nanosheet active sites showcased a perfect blend, emphasizing that both multi-metal and carbon active centers play a crucial role in achieving high ORR electrocatalytic activity.

The introduction of 2 mL of 0.1 M KH_2PO_4 to a 0.1 M KOH electrolyte solution led to a reduction in current for $NiFe_2O_4$/PCNS and $NiFe_2O_4$/NCNS. However, the decrease was not pronounced, suggesting a weaker synergy between metal and carbon active centers in these hybrid electrocatalysts. In contrast to the complex spinel nickel ferrite on NPCNS, $NiFe_2O_4$ on NCNS/PCNS might be an inverse spinel structure that does not rely heavily on carbon supports for formation [14,54–57].

4. Conclusion

In summary, a successful synthesis of complex spinel $NiFe_2O_4$ nanoparticles anchored on nitrogen and phosphorus co-doped carbon nanosheets using a combination of sol-gel and carbonization methods was reported for the first time to be active for ORR in alkaline media. The resulting material exhibited uniform dispersion, excellent CO-tolerance, and outstanding electrochemical activity. The synergistic effect between the crystalline structure of complex spinel $NiFe_2O_4$ and NPCNS contributed to enhanced ORR activity, selectivity, and durability. Electrochemical analysis revealed that $NiFe_2O_4$/NPCNS surpassed 20 % Pt/C and other electrocatalysts in terms of high current density (7.81 mA/cm^2), high onset potential (0.92 V vs RHE), low charge transfer resistance (41.13 Ω), and minimal Tafel slope (87.0 mV/dec). Additionally, $NiFe_2O_4$/NPCNS demonstrated exceptional resilience to poisoning and negligible deactivation rates in chronoamperometry and cyclic studies, highlighting its superior long-term stability and durability. Elevated temperatures (1000 °C) where proven to cause partial oxidation of nickel on the surface of $NiFe_2O_4$/NPCNS which transformed the nickel ferrite from an inverse spinel structure to a complex spinel structure. The exceptional performance of $NiFe_2O_4$/NPCNS is attributed to the synergistic combination of Ni^{2+}, Ni^{3+}, Fe^{2+}, and Fe^{3+} ions on a complex spinel structure, coupled with the electrical interaction between these metals and heteroatoms on the carbon matrix. The doping strategy creates additional active sites on the carbon surface, facilitating oxygen molecule adsorption and enhancing ORR kinetics. Future prospects for this unique material will be to refine the synthetic method to only favour the synthesis of complex spinel $NiFe_2O_4$ by modulating the synthetic precursors (ratios etc), to favour the formation of that structure. Varying the temperature from 700^{o}C to 1000 °C during the synthesis process can also be explored to pinpoint the exact temperature where the $NiFe_2O_4$ spinel ferrite transitions from an inverse spinel structure to a complex spinel structure.

Data availability statement

The data that support this study are available from the corresponding author upon reasonable request.

CRediT authorship contribution statement

Siyabonga Patrick Mbokazi: Writing – original draft, Visualization, Validation, Methodology, Investigation, Formal analysis, Data curation, Conceptualization. **Thabo Matthews:** Writing – review & editing, Visualization, Validation, Investigation. **Haitao Zheng:** Writing – review & editing, Visualization, Validation, Methodology, Investigation. **Makhaokane Paulina Chabalala:** Writing – review & editing, Data curation. **Memory Zikhali:** Writing – review & editing. **Kudzai Mugadza:** Validation, Investigation. **Sandile Gwebu:** Writing – original draft, Validation. **Lukhanyo Mekuto:** Writing – review & editing, Visualization, Supervision, Methodology, Funding acquisition, Conceptualization. **Nobanathi Wendy Maxakato:** Writing – review & editing, Visualization, Supervision, Methodology, Funding acquisition, Conceptualization.

Declaration of competing interest

The authors declare that they have no known competing financial interests or personal relationships that could have appeared to influence the work reported in this paper.

Acknowledgments

This research was funded by the National Research Foundation of South Africa: Grant Number 118148. National Research Foundation of South Africa: Grant Number 138083. The Centre for Nanomaterials Science Research (CNSR), University of Johannesburg. The University of Johannesburg Research Council (URC) and the National Research Foundation of South Africa, Postgraduate Scholarship (2021–2023) for financial support and the Faculty of Science, Department of Chemical Sciences at the University of Johannesburg, South Africa.

Appendix. ASupplementary data

Supplementary data to this article can be found online at https://doi.org/10.1016/j.heliyon.2024.e35483.

References

[1] T. Ling, D.Y. Yan, Y. Jiao, H. Wang, Y. Zheng, X. Zheng, J. Mao, X.W. Du, Z. Hu, M. Jaroniec, S.Z. Qiao, Engineering surface atomic structure of single-crystal cobalt (II) oxide nanorods for superior electrocatalysis, Nat. Commun. 7 (2016) 12876, https://doi.org/10.1038/ncomms12876.

[2] F. Cheng, J. Chen, Metal–air batteries: from oxygen reduction electrochemistry to cathode catalysts, Chem. Soc. Rev. 41 (2012) 2172–2192, https://doi.org/10.1039/C1CS15228A.

[3] S. Ren, S. Ma, Y. Yang, Q. Mao, C. Hao, Hydrothermal synthesis of Fe_2O_3/polypyrrole/graphene oxide composites as highly efficient electrocatalysts for oxygen reduction reaction in alkaline electrolyte, *178*, Electrochim. Acta (2015) 179–189, https://doi.org/10.1016/j.electacta.2015.07.181.

[4] F. Xian, L. Gao, Z. Zhang, H. Zhang, S. Dong, G. Cui, N, P dual-doped multi-wrinkled nanosheets prepared from the egg crude lecithin as the efficient metal-free electrocatalyst for oxygen reduction reaction, Appl. Surf. Sci. 476 (2019) 76–83, https://doi.org/10.1016/j.apsusc.2018.12.293.

[5] J. Zhang, L. Dai, Nitrogen, phosphorus, and fluorine tri-doped graphene as a multifunctional catalyst for self-powered electrochemical water splitting, Angew. Chem. Int. Ed. 128 (2016) 13490–13494, https://doi.org/10.1002/ange.201607405.

[6] C. Huang, T. Ouyang, Y. Zou, N. Li, Z.Q. Liu, Ultrathin $NiCo_2P_x$ nanosheets strongly coupled with CNTs as efficient and robust electrocatalysts for overall water splitting, *6*, J. Mater. Chem. A Mater. (2018) 7420–7427, https://doi.org/10.1039/C7TA11364A.

[7] W. Bi, X. Li, R. You, M. Chen, R. Yuan, W. Huang, X. Wu, W. Chu, C. Wu, Y. Xie, Surface immobilization of transition metal ions on nitrogen-doped graphene realizing high-efficient and selective CO_2 reduction, *30*, Adv. Mater. (2018) 1706617, https://doi.org/10.1002/adma.201706617.

[8] S. Gao, X. Li, L. Li, X. Wei, A versatile biomass derived carbon material for oxygen reduction reaction, supercapacitors and oil/water separation, *33*, Nano Energy (2017) 334–342, https://doi.org/10.1016/j.nanoen.2017.01.045.

[9] S. Peng, L. Li, Y. Hu, M. Srinivasan, F. Cheng, J. Chen, S. Ramakrishna, Fabrication of spinel one-dimensional architectures by single-spinneret electrospinning for energy storage applications, *9*, ACS Nano (2015) 1945–1954, https://doi.org/10.1021/nn506851x.

[10] H. Wu, J. Geng, H. Ge, Z. Guo, Y. Wang, G. Zheng, Egg-derived mesoporous carbon microspheres as bifunctional oxygen evolution and oxygen reduction electrocatalysts, *6*, Adv. Energy Mater. (2016) 1600794, https://doi.org/10.1002/aenm.201600794.

[11] T. Matthews, T.H. Dolla, S.S. Gwebu, T.A. Mashola, L.T. Dlamini, E. Carleschi, P. Ndungu, N.W. Maxakato, Mn-Ni-Co-O spinel oxides towards oxygen reduction reaction in alkaline medium: $Mn_{0.5}Ni_{0.5}Co_2O_4$/C synergism and cooperation, *11*, Catalysts (2021) 1059, https://doi.org/10.3390/catal11091059.

[12] S.G. Mohamed, Y.Q. Tsai, C.J. Chen, Y.T. Tsai, T.F. Hung, W.S. Chang, R.S. Liu, Ternary spinel MCo_2O_4 (M = Mn, Fe, Ni, and Zn) porous nanorods as bifunctional cathode materials for lithium–O_2 batteries, *7*, ACS Appl. Mater. Interfaces (2015) 12038–12046, https://doi.org/10.1021/acsami.5b02180.

[13] P. Li, R. Ma, Y. Zhou, Y. Chen, Q. Liu, G. Peng, Z. Liang, J. Wang, Spinel nickel ferrite nanoparticles strongly cross-linked with multiwalled carbon nanotubes as a bi-efficient electrocatalyst for oxygen reduction and oxygen evolution, *5*, RSC Adv. (2015) 73834–73841, https://doi.org/10.1039/C5RA14713A.

[14] J.Y. Qin, S. Wang, S. Zhou, T. Liu, Y. Yin, J. Yang, Dominating role of interfacial N–Ni coordination in spinel nickel ferrite/N-doped graphene hybrids for boosting reversible oxygen electrocatalysis, *2*, Adv. Energy Sustain. Res. (2021) 2000106, https://doi.org/10.1002/aesr.202000106.

[15] M. Kiani, J. Zhang, J. Chen, Y. Luo, Y. Chen, J. Fan, G. Wang, R. Wang, Facile synthesis of magnesium ferrite nanoparticles supported on nitrogen and sulfur co-doped carbon black as an efficient electrocatalyst for oxygen reduction reaction, *21*, J. Nanoparticle Res. (2019) 1–12, https://doi.org/10.1007/s11051-019-4539-9.

[16] P. Gokuladeepan, A. Karthigeyan, Effect of annealing temperature on oxygen reduction reaction of reduced graphene oxide incorporated cobalt oxide nanocomposites for fuel cell applications, *449*, Appl. Surf. Sci. (2018) 705–711, https://doi.org/10.1016/j.apsusc.2017.12.153.

[17] J. Zhang, M. Lv, D. Liu, L. Du, Z. Liang, Nitrogen-doped carbon nanoflower with superior ORR performance in both alkaline and acidic electrolyte and enhanced durability, *43*, Int. J. Hydrogen Energy (2018) 4311–4320, https://doi.org/10.1016/j.ijhydene.2017.12.147.

[18] J. Liu, T. Zhang, Z. Wang, G. Dawson, W. Chen, Simple pyrolysis of urea into graphitic carbon nitride with recyclable adsorption and photocatalytic activity, *21*, J. Mater. Chem. (2011) 14398–14401, https://doi.org/10.1039/C1JM12620B.

[19] A. Kumar, P. Kumar, C. Joshi, M. Manchanda, R. Boukherroub, S.L. Jain, Nickel decorated on phosphorous-doped carbon nitride as an efficient photocatalyst for reduction of nitrobenzenes, *6*, Nanomaterials (2016) 59, https://doi.org/10.3390/nano6040059.

[20] D.H. Chen, S.H. Wu, Synthesis of nickel nanoparticles in water-in-oil microemulsions, *12*, Chem. Mater. (2000) 1354–1360, https://doi.org/10.1021/cm991167y.

[21] Z. Ma, X. Huang, S. Dou, J. Wu, S. Wang, One-pot synthesis of Fe_2O_3 nanoparticles on nitrogen-doped graphene as advanced supercapacitor electrode materials, *118*, J. Phys. Chem. C (2014) 17231–17239, https://doi.org/10.1021/jp502226j.

[22] S. Eigler, C. Dotzer, A. Hirsch, M. Enzelberger, P. Muller, Formation and decomposition of CO_2 intercalated graphene oxide, *24*, Chem. Mater. (2012) 1276–1282, https://doi.org/10.1021/cm203223z.

[23] M. Kiani, J. Zhang, J. Fan, H. Yang, G. Wang, J. Chen, R. Wang, Spinel nickel ferrite nanoparticles supported on nitrogen doped graphene as efficient electrocatalyst for oxygen reduction in fuel cells, *7*, Mater. Express (2017) 261–272, https://doi.org/10.1166/mex.2017.1376.

[24] A. Pisanu, A. Speltini, B. Vigani, F. Ferrari, M. Mannini, N. Calisi, B. Cortigiani, A. Caneschi, P. Quadrelli, A. Profumo, L. Malavasi, Enhanced hydrogen photogeneration by bulk gC_3N_4 through a simple and efficient oxidation route, Dalton Trans. 47 (2018) 6772–6778, https://doi.org/10.1039/C8DT00276B.

[25] J. Rouquerol, D. Avnir, C.W. Fairbridge, D.H. Everett, J.M. Haynes, N. Pernicone, J.D. Ramsay, K.S. Sing, K.K. Unger, Recommendations for the characterization of porous solids (Technical Report), *66*, Pure Appl. Chem. (1994) 1739–1758, https://doi.org/10.1351/pac199466081739.

[26] B. Wang, W. Al Abdulla, D. Wang, X.S. Zhao, A three-dimensional porous $LiFePO_4$ cathode material modified with a nitrogen-doped graphene aerogel for high-power lithium ion batteries, *8*, Energy Environ. Sci. (2015) 869–875, https://doi.org/10.1039/C4EE03825H.

[27] C.M. Doherty, R.A. Caruso, C.J. Drummond, High performance $LiFePO_4$ electrode materials: influence of colloidal particle morphology and porosity on lithium-ion battery power capability, *3*, Energy Environ. Sci. (2010) 813–823, https://doi.org/10.1039/B922898E.

[28] Y. Wang, W. Chen, Y. Nie, L. Peng, W. Ding, S. Chen, L. Li, Z. Wei, Construction of a porous nitrogen-doped carbon nanotube with open-ended channels to effectively utilize the active sites for excellent oxygen reduction reaction activity, *53*, Chem. Commun. (2017) 11426–11429, https://doi.org/10.1039/C7CC07249J.

[29] S. Guo, P. Yuan, J. Zhang, P. Jin, H. Sun, K. Lei, X. Pang, Q. Xu, F. Cheng, Atomic-scaled cobalt encapsulated in P,N-doped carbon sheaths over carbon nanotubes for enhanced oxygen reduction electrocatalysis under acidic and alkaline media, *53*, Chem. Commun. (2017) 9862–9865, https://doi.org/10.1039/C7CC05476A.

[30] B. Lesiak, L. Kövér, J. Tóth, J. Zemek, P. Jiricek, A. Kromka, N.J. Rangam, C sp^2/sp^3 hybridisations in carbon nanomaterials–XPS and (X) AES study, *452*, Appl. Surf. Sci. (2018) 223–231, https://doi.org/10.1016/j.apsusc.2018.04.269.

[31] Z. Lin, M. Song, Y. Ding, Y. Liu, M. Liu, C. Wong, Facile preparation of nitrogen-doped graphene as a metal-free catalyst for oxygen reduction reaction, *14*, Phys. Chem. Chem. Phys. (2012) 3381–3387, https://doi.org/10.1039/C2CP00032F.

[32] H. Yin, C. Zhang, F. Liu, Y. Hou, Hybrid of iron nitride and nitrogen-doped graphene aerogel as synergistic catalyst for oxygen reduction reaction, *24*, Adv. Funct. Mater. (2014) 2930–2937, https://doi.org/10.1002/adfm.201303902.

[33] T. Panja, D. Bhattacharjya, J.S. Yu, Nitrogen and phosphorus co-doped cubic ordered mesoporous carbon as a supercapacitor electrode material with extraordinary cyclic stability, *3*, J. Mater. Chem. A Mater. (2015) 18001–18009, https://doi.org/10.1039/C5TA04169D.

[34] W. Wang, J. Li, Y. Kang, F. Wang, J. Song, Z. Lei, Facile and scalable preparation of nitrogen, phosphorus codoped nanoporous carbon as oxygen reduction reaction electrocatalyst, *248*, Electrochim. Acta (2017) 11–19, https://doi.org/10.1016/j.electacta.2017.07.033.

[35] Y. Li, S. Li, Y. Wang, J. Wang, H. Liu, X. Liu, L. Wang, X. Liu, W. Xue, N. Ma, Electrochemical synthesis of phosphorus-doped graphene quantum dots for free radical scavenging, *19*, Phys. Chem. Chem. Phys. (2017) 11631–11638, https://doi.org/10.1039/C6CP06377B.

[36] L. Qu, Z. Wang, X. Hou, J. Mao, S. Wang, G. Sun, Y. Wu, X. Liu, "Rose Flowers" assembled from mesoporous $NiFe_2O_4$ nanosheets for energy storage devices, 28, J. Mater. Sci. Mater. Electron. (2017) 14058–14068, https://doi.org/10.1007/s10854-017-7257-z.

[37] J.K. Dey, A. Chatterjee, S. Majumdar, A.C. Dippel, O. Gutowski, M.V. Zimmermann, S. Giri, Ferroelectric order associated with ordered occupancy at the octahedral site of the inverse spinel structure of multiferroic $NiFe_2O_4$, *99*, Phys. Rev. B (2019) 144412, https://doi.org/10.1103/PhysRevB.99.144412.

[38] Z. Mojović, T. Mudrinić, P. Banković, N. Jović-Jovičić, A. Ivanović-Šašić, A. Milutinović-Nikolić, D. Jovanović, Oxygen reduction reaction on palladium-modified zeolite 13X, *19*, J. Solid State Electrochem. (2015) 1993–2000, https://doi.org/10.1007/s10008-014-2724-4.

[39] L. Jiao, Y. Hu, H. Ju, C. Wang, M.R. Gao, Q. Yang, J. Zhu, S.H. Yu, H.L. Jiang, From covalent triazine-based frameworks to N-doped porous carbon/reduced graphene oxide nanosheets: efficient electrocatalysts for oxygen reduction, *5*, J Mater. Chem. A Mater (2017) 23170–23178, https://doi.org/10.1039/C7TA07387A.

[40] B. Liang, S. Guo, Y. Zhao, I.U. Khan, X. Zhang, K. Li, C. Lv, Single iron atoms anchored on activated carbon as active centres for highly efficient oxygen reduction reaction in air-cathode microbial fuel cell, *450*, J. Power Sources (2020) 227683, https://doi.org/10.1016/j.jpowsour.2019.227683.

[41] E. Cossar, M.S.E. Houache, Z. Zhang, E.A. Baranova, Comparison of electrochemical active surface area methods for various nickel nanostructures, 870, J. Electroanal. Chem (2020) 114246, https://doi.org/10.1016/j.jelechem.2020.114246.

[42] G. Song, H. Yang, Y. Sun, J. Wang, W. Qu, Q. Zhang, L. Ma, Y. Feng, The catalytic effect of iron oxide on the oxidation of methanol by platinum in alkaline media, *38*, Chin. J. Catal. (2017) 554–562, https://doi.org/10.1016/S1872-2067(17)62773-6.

[43] M.A.A. Rahim, R.M.A. Hameed, M.W. Khalil, Nickel as a catalyst for the electro-oxidation of methanol in alkaline medium, *134*, J. Power Sources (2004) 160–169, https://doi.org/10.1016/j.jpowsour.2004.02.034.

[44] M. Lei, J. Wang, J.R. Li, Y.G. Wang, H.L. Tang, W.J. Wang, Emerging methanol-tolerant AlN nanowire oxygen reduction electrocatalyst for alkaline direct methanol fuel cell, *4*, Sci. Rep. (2014) 6013, https://doi.org/10.1038/srep06013.

[45] Y. Feng, N. Alonso-Vante, Nonprecious metal catalysts for the molecular oxygen-reduction reaction, *245*, Phys. Status Solidi (2008) 1792–1806, https://doi.org/10.1002/pssb.200879537.

[46] S. Sohrabi, M. Ghalkhani, S. Dehghanpour, The electrocatalytic stability investigation of a proton manager MOF for the oxygen reduction reaction in acidic media, *29*, J. Inorg. Organomet. Polym. Mater. (2019) 528–534, https://doi.org/10.1007/s10904-018-1025-2.

[47] O.V. Kharissova, B.I. Kharisov, Variations of interlayer spacing in carbon nanotubes, *4*, RSC Adv. (2014) 30807–30815, https://doi.org/10.1039/C4RA04201H.

[48] J. Hwang, A. Ejsmont, R. Freund, J. Goscianska, B.V.K.J. Schmidt, S. Wuttke, Controlling the morphology of metal–organic frameworks and porous carbon materials: metal oxides as primary architecture-directing agents, *49*, Chem. Soc. Rev. (2020) 3348–3422, https://doi.org/10.1039/C9CS00871C.

[49] L. Liu, X. Du, Polyethylenimine-modified graphitic carbon nitride nanosheets: a label-free Raman traceable siRNA delivery system, *9*, J. Mater. Chem. B (2021) 6895–6901, https://doi.org/10.1039/D1TB00984B.

[50] X. Xie, M. Chen, S. Zhai, F. Wang, Eutectic metal+ troilite+ Fe-Mn-Na phosphate+ Al-free chromite assemblage in shock-produced chondritic melt of the Yanzhuang chondrite, 49, Meteorit. Planet. Sci (2014) 2290–2304, https://doi.org/10.1111/maps.12379.

[51] D.H. Kweon, M.S. Okyay, S.J. Kim, J.P. Jeon, H.J. Noh, N. Park, J. Mahmood, J.B. Baek, Ruthenium anchored on carbon nanotube electrocatalyst for hydrogen production with enhanced Faradaic efficiency, *11*, Nat. Commun. (2020) 1278, https://doi.org/10.1038/s41467-020-15069-3.

[52] H.A. Bandal, A.A. Pawar, H. Kim, Transformation of waste onion peels into core-shell Fe3C@ N-doped carbon as a robust electrocatalyst for oxygen evolution reaction, *422*, Electrochim. Acta (2022) 140545, https://doi.org/10.1016/j.electacta.2022.140545.

[53] S. Vasudevan, J. Lakshmi, The adsorption of phosphate by graphene from aqueous solution, *2*, RSC Adv. (2012) 5234–5242, https://doi.org/10.1039/C2RA20270K.

[54] T. Tang, Y. Wang, J. Han, Q. Zhang, X. Bai, X. Niu, Z. Wang, J. Guan, Dual-atom Co-Fe catalysts for oxygen reduction reaction, *46*, Chin. J. Catal. (2023) 48–55, https://doi.org/10.1016/S1872-2067(22)64189-5.

[55] T. Tang, Z. Wang, J. Guan, Structural optimization of carbon-based diatomic catalysts towards advanced electrocatalysis, Coord. Chem. Rev. 492 (2023) 215288, https://doi.org/10.1016/j.ccr.2023.215288.

[56] X. Bai, Y. Wang, J. Han, X. Niu, J. Guan, Engineering the electronic structure of isolated manganese sites to improve the oxygen reduction, Zn-air battery and fuel cell performances, *337*, Appl. Catal., B (2023) 122966, https://doi.org/10.1016/j.apcatb.2023.122966.

[57] Y. Qin, C. Guo, Z. Ou, C. Xu, Q. Lan, R. Jin, Y. Liu, Y. Niu, Q. Xu, Y. Si, H. Li, Regulating single-atom Mn sites by precisely axial pyridinic-nitrogen coordination to stabilize the oxygen reduction, *80*, J. Energy Chem. (2023) 542–552, https://doi.org/10.1016/j.jechem.2023.01.048.

[58] M. Singh, A. Rai, V.K. Rai, Electrocatalysis: application of nanocomposite materials. Methods for Electrocatalysis: Advanced Materials and Allied Applications, 2020, pp. 113–123, https://doi.org/10.1007/978-3-030-27161-9_4.

[59] C. Sedrati, S. Alleg, H. Boussafel, A. Bendali Hacine, Structure and magnetic properties of nickel ferrites synthesized by a facile co-precipitation method: effect of the Fe/Ni ratio, *32*, J. Mater. Sci. Mater. Electron. (2021) 24548–24559, https://doi.org/10.1007/s10854-021-06932-0.

[60] J. Kumar, C.R. Mariappan, V. Kumar, S. Murugavel, G.V. Prakash, Study of spinel-type $ZnNi_xCo_{2x}O_4$ nano-particles, synthesised by thermal decomposition of ternary metal nitrate solutions, *83*, Mater. Res. Bull. (2016) 632–639, https://doi.org/10.1016/j.materresbull.2016.07.011.

[61] G. Song, H. Yang, Y. Sun, J. Wang, W. Qu, Q. Zhang, L. Ma, Y. Feng, Promoting effects of Fe_2O_3 to Pt electrocatalysts toward methanol oxidation reaction in alkaline electrolyte, 38, Chin. J. Catal (2017) 554–562, https://doi.org/10.1016/S1872-2067(17)62773-6.

[62] H. Qin, Y. He, P. Xu, H. Huang, Z. Wang, H. Wang, Z. Wang, Y. Zhao, Q. Tian, C. Wang, Wang Spinel ferrites (MFe_2O_4): synthesis, improvement and catalytic application in environment and energy field, Adv. Colloid Interface Sci. 294 (2021) 102486, https://doi.org/10.1016/j.cis.2021.102486.

[63] Y. Go, K. Min, H. An, K. Kim, S.E. Shim, S.H. Baeck, Oxygen-vacancy-rich CoFe/$CoFe_2O_4$ embedded in N-doped hollow carbon spheres as a highly efficient bifunctional electrocatalyst for Zn–air batteries, Chem. Eng. J. 448 (2022) 137665, https://doi.org/10.1016/j.cej.2022.137665.

[64] S.V. Bhandare, R. Kumar, A.V. Anupama, H.K. Choudhary, V.M. Jali, B. Sahoo, Mechanistic insights into the sol-gel synthesis of complex (quaternary) Co–Mn–Zn-spinel ferrites: an annealing dependent study, *46*, Ceram. Int. (2020) 17400–17415, https://doi.org/10.1016/j.ceramint.2020.04.031.

[65] G. Zhang, G. Li, X. Wang, Surface modification of carbon nitride polymers by core–shell nickel/nickel oxide cocatalysts for hydrogen evolution photocatalysis, *7*, ChemCatChem (2015) 2864–2870, https://doi.org/10.1002/cctc.201500069.

[66] O. Alduhaish, M. Ubaidullah, A.M. Al-Enizi, N. Alhokbany, S.M. Alshehri, J. Ahmed, Facile synthesis of mesoporous α-Fe_2O_3@ g-C_3N_4-NCs for efficient bifunctional electro-catalytic activity (OER/ORR), *9*, Sci. Rep. (2019) 14139, https://doi.org/10.1038/s41598-019-50780-2.

[67] J. Lilloja, E. Kibena-Põldsepp, E. Kibena-Põldsepp, A. Sarapuu, J.C. Douglin, M. Käärik, J. Kozlova, P. Paiste, A. Kikas, J. Aruväli, J. Leis, V. Sammelselg, D. R. Dekel, K. Tammeveski, Transition-metal- and nitrogen-doped carbide-derived carbon/carbon nanotube composites as cathode catalysts for anion-exchange membrane fuel cells, *11*, ACS Catal. (2021) 1920–1931, https://doi.org/10.1021/acscatal.0c03511.

[68] J. Jiang, X.X. Liu, J. Han, K. Hu, J.S. Chen, Self-supported sheets-on-wire CuO@ Ni $(OH)_2$/$Zn(OH)_2$ nanoarrays for high-performance flexible quasi-solid-state supercapacitor, *9*, Processes (2021) 680, https://doi.org/10.3390/pr9040680.

[69] Y. Liu, L. Xiao, H. Tan, J. Zhang, C. Dong, H. Liu, X. Du, J. Yang, Amorphous/crystalline phases mixed nanosheets array rich in oxygen vacancies boost oxygen evolution reaction of spinel oxides in alkaline media, Small (2024) (2024) 2401504, https://doi.org/10.1002/smll.202401504.

[70] L. Lu, Q. Hao, W. Lei, X. Xia, P. Liu, D. Sun, X. Wang, X. Yang, Well-combined magnetically separable hybrid cobalt ferrite/nitrogen-doped graphene as efficient catalyst with superior performance for oxygen reduction reaction, Small 11 (2015) 5833–5843, https://doi.org/10.1002/smll.201502322.

[71] Q. Huang, C. Li, Y. Tu, Y. Jiang, P. Mei, X. Yan, Spinel $CoFe_2O_4$/carbon nanotube composites as efficient bifunctional electrocatalysts for oxygen reduction and oxygen evolution reaction, *47*, Ceram. Int. (2021) 1602–1608, https://doi.org/10.1016/j.ceramint.2020.08.276.

[72] M. Qian, X. Cheng, T. Sun, J. Tian, T.T. Isimjan, Z.F. Shi, X. Yang, Synergistic catalytic effect of N-doped carbon embedded with CoFe-rich $CoFe_2O_4$ clusters as highly efficient catalyst towards oxygen reduction, *819*, J. Alloys Compd. (2020) 153015, https://doi.org/10.1016/j.jallcom.2019.153015.

[73] J.X. Flores-Lasluisa, D. Salinas-Torres, M.V. Lopez-Ram, M.A. Alvarez, C. Moreno-Castilla, D. Cazorla-Amoros, E. Morallon, Copper ferrite nanospheres composites mixed with carbon black to boost the oxygen reduction reaction, 613, Colloid. Surf. A Physicochem. Eng.

[74] Q. Jing, Z. Mei, X. Sheng, X. Zou, Y. Yang, C. Zhang, L. Wang, Y. Sun, L. Duan, H. Guo, 3d orbital electron engineering in oxygen electrocatalyst for zinc-air batteries, 462, Chem. Eng. J. (2023) 142321, https://doi.org/10.1016/j.cej.2023.142321.

[75] Y. Sun, X. Ren, S. Sun, Z. Liu, S. Xi, Z.J. Xu, Engineering high-spin state cobalt cations in spinel zinc cobalt oxide for spin channel propagation and active site enhancement in water oxidation, 133, Angew. Chem. Int. Ed. (2021) 14657–14665, https://doi.org/10.1002/ange.202102452.

[76] S. Gupta, W. Kellogg, H. Xu, X. Liu, J. Cho, G. Wu, Bifunctional perovskite oxide catalysts for oxygen reduction and evolution in alkaline media, 11, Chem. Asian J. (2016) 10–21, https://doi.org/10.1002/asia.201500640.

[77] Z. Zhao, P.K. Shen, Mechanism of oxygen reduction reaction. Electrochemical Oxygen Reduction: Fundamental and Applications, Springer, Singapore, 2021, pp. 11–27, https://doi.org/10.1007/978-981-33-6077-8_2.